Nonlinear Dynamics (2026) 114:244
https://doi.org/10.1007/s11071-025-12114-y

RESEARCH

Markovian spectral transition modeling with temporal dependencies for railway bogie axle bearing diagnostics in non-stationary transient environments

Peng Chen[1,2] · Junxiao Ma[1] · Jia Gao[1] · Ge Xin[3] · Changbo He[4]

Received: 8 July 2025 / Revised: 26 October 2025 / Accepted: 1 December 2025

Abstract

In real-world scenarios, railway bogie axle bearing diagnostic techniques face significant limitations in handling non-stationary operational conditions and multiple interfering noise sources, particularly in complex railway environments. Traditional approaches exhibit insufficient robustness and require complex post-processing strategies, especially when confronted with multivariate random pulse noise typical in railway operations. To address these challenges, this study proposes a novel Markovian spectral transition modeling framework with temporal dependencies, specifically designed for railway bogie axle bearing diagnostics in non-stationary transient environments. The framework introduces an innovative integration of Markovian modeling with multi-resolution wavelet analysis, alongside an amplitude-adaptive interference suppression mechanism that employs statistical signal modeling for dynamic thresholding. This comprehensive diagnostic methodology uniquely combines multiple signal processing techniques to handle transient interference noise in non-stationary bearing signals, leveraging intrinsic signal properties to enhance demodulation robustness. The proposed framework systematically integrates wavelet coefficients into Markovian state representations, establishing theoretical foundations for parameter optimization and providing a structured approach to railway bearing fault detection. The methodology demonstrates significant potential in advancing railway bogie axle bearing diagnostics, particularly in challenging operational environments characterized by complex noise patterns and non-stationary conditions typical of railway systems.

Keywords Railway locomotive · Bogie axle bearing · Fault diagnosis · Vibration signal processing · Non-stationary operating condition

Signal and General Processing

$x(t)$, $x[n]$	The original continuous-time and discrete-time vibration signal.
M	Length of the sliding window.
h	Hop size (shift) of the sliding window.
w	Rectangular window function.
m_d	Threshold for local peak detection.
N_p	Number of local peaks detected within a window.

Wavelet Analysis

$\phi_{j,k}(t)$, $\psi_{j,k}(t)$	Scaling function and wavelet function at scale j and shift k.
$cA_{j,k}$	Approximation coefficients at decomposition level j.
$cD_{j,k}$	Detail coefficients at decomposition level j.
$h[n]$, $g[n]$	Low-pass and high-pass filter coefficients for the wavelet transform.
ε	Soft-threshold value applied to detail coefficients.
q	Percentage parameter for calculating ε (set to 0.1).

✉ Ge Xin
ge.xin@bjtu.edu.cn

Peng Chen
pengchen@alu.uestc.edu.cn, dr.pengchen@foxmail.com

[1] College of Engineering, Shantou University, Shantou 515063, Guangdong, People's Republic of China

[2] Key Laboratory of Intelligent Manufacturing Technology, Shantou University, Shantou 515063, Guangdong, People's Republic of China

[3] School of Traffic and Transportation, Beijing Jiaotong University, Beijing 100044, People's Republic of China

[4] College of Electrical Engineering and Automation, Anhui University, Hefei 230601, Anhui, People's Republic of China

Published online: 24 February 2026

$\hat{x}(t)$	The reconstructed signal after wavelet processing.
τ	Mean of the original signal, used for peak preservation.
Π	Set of indices identifying significant peaks in the signal.

Markov Modeling

S_i, S_j	Discrete state of the signal at time i or a general state j.
n_{bin}	Total number of discrete states/bins (set to 10).
Δ	Width of each amplitude bin.
N_{ij}^{MTM}	Markov Transition Matrix, counting transitions from state i to j.
$\delta(\cdot)$	Kronecker delta function (returns 1 if arguments are equal, else 0).
θ	Threshold for pruning high-frequency transitions in the MTM.
α	Ratio parameter for calculating θ (set to 0.1).
P_{ij}	Markov Transition Probability Matrix, the normalized probability from state i to j.

Proposed MLFTPR-PM Framework

f_i	A key frequency component identified from the FFT.
p_i	Period corresponding to the key frequency f_i.
$C_i(t)$	Set of valid sampling indices for period p_i at time t.
$\bar{x}_{p_i}$	Periodic mean, the baseline signal level for period p_i.
$Amp(f_i)$	Amplitude of the frequency component f_i.
w_i	Weight for period p_i, proportional to its amplitude.
τ_{markov}	The final weighted periodic threshold for anomaly detection.
$\mathbb{1}\{\cdot\}$	Indicator function (returns 1 if condition is true, else 0).
λ	Average value of the MLFTPR-PM metric across the signal.
γ	Coefficient for determining anomaly boundaries based on λ.
Ω	Set of identified anomaly boundaries.
y_{lim}^{i}	Final predicted value with amplitude interference limitation.

1 Introduction

The high-speed train represents a sophisticated and intricately coupled mechanical system, wherein the bogie system serves as a critical component of the railway rolling stock that fundamentally influences the operational safety and reliability of train movements [1]. Within this complex system, bogie axle bearings, which operate under persistently demanding conditions characterized by substantial loads and multifaceted environmental stressors during prolonged high-speed operations, are particularly susceptible to progressive wear, deterioration, and potential mechanical damage. Given that bogie axle bearing failures can precipitate catastrophic consequences for railway operations and passenger safety, it is imperative to implement comprehensive fault monitoring protocols and develop predictive maintenance strategies. These proactive measures are essential for ensuring the sustained operational integrity of locomotive systems and preventing potentially hazardous situations that could compromise railway safety standards.

The detection and diagnostics of faults in bogie axle bearing within bogie systems are primarily undertaken using two distinct methodologies: vibration signal processing [2–5] and deep learning strategies [6–10]. Vibration signal processing involves the analysis of bogie axle bearing vibrations to identify distinguishing characteristics that serve as indicators of potential faults. Researchers employ techniques across the time domain [3, 11], frequency domain [8, 12, 13], and time-frequency domain [14] to extract meaningful and interpretable features. These conventional methods are particularly advantageous in scenarios where large datasets are unavailable, as they are reliable under data constraints and allow experts to derive insights directly from the extracted features. On the other hand, deep learning approaches leverage advanced algorithms, such as Convolutional Neural Networks (CNN) [15, 16], Recurrent Neural Network (RNN) [17], and Transformers [18], to analyze vibration signals. These models are adept at identifying subtle patterns and capturing complex, nonlinear relationships that traditional methods might overlook. Despite their superior capability in recognizing intricate fault characteristics, deep learning models face challenges. They typically require vast amounts of data to train effectively and often operate as "black box" systems, offering limited transparency in their decision-making processes. Furthermore, collecting labeled datasets for bogie axle bearings functioning under real-world operating conditions is particularly challenging due to data sparsity, which adds another layer of difficulty when applying deep learning to these diagnostic tasks.

A fundamental challenge in data-driven diagnostics is the performance degradation caused by Environmental and Operational Variabilities (EOVs), which induce distribution shifts in vibration data. As demonstrated by recent research, such as the WaveCORAL-DCCA framework for rotor fault diagnosis [19], domain adaptation provides a powerful strategy to mitigate these shifts. While such contemporary solutions often rely on deep learning, this reliance is not obligatory.

A key challenge in bearing fault diagnosis is detecting damage-indicative signals—characterized by repetitive time-domain peaks and component-specific frequency-domain signatures—amid noise. Spectral Kurtosis (SK) and the Kurtogram [20] advanced this field, but SK-based bandwidth division remains vulnerable to external disturbances, hindering differentiation between faults and noise.

Fault diagnosis techniques have evolved to address core challenges in complex environments. To tackle non-Gaussian noise and high-energy pulses, Barszcz and Jabło'nski proposed an enhanced Kurtogram that prioritizes cyclostationarity over impulsiveness, improving diagnostic reliability. This spurred more advanced frameworks: Han et al.'s ACYCBD$_\beta$ [21] extracts fault signals from high-speed train bearings under noise without prior fault period knowledge; Hou et al. [22] integrated the fault characteristic signal-to-noise ratio (FCSNR) to strengthen fault identification in real-world noisy conditions; and Wang et al. [23] and He et al. [24] developed Ensefgram—using adaptive filters and the composite statistical index (ENSEF)—to optimize demodulation bands and boost diagnosis accuracy.

Current SK-based bandwidth selection methods remain sensitive to external disturbances, leading to false positives or missed detections in dynamic environments. To address this, Pancaldi et al. [25] created a simulation framework (modeling wideband/narrowband noise) to objectively evaluate rolling bearing fault algorithms. Yang et al. [26] introduced the harmonic noise kurtosis-time characteristic blind deconvolution (HTBD) methodology, combining integration of harmonic noise kurtosis (HNK) and time characteristic energy ratio (TCER) to enhance fault period identification accuracy and stability; meanwhile, Peng et al. [27] advanced CYCBD$_\beta$ with a generalized Gaussian cyclostationarity model, improving fault feature extraction under strong non-Gaussian noise.

Chen et al. [28] designed an adaptive framework for wind turbine bearing diagnosis (with Dynamic Markov Transition Frequency with Adaptive Peak Rates (DMTF-APR) and Multi-Period Weighted Average Framework (MPWAF)), and Gabor et al. [29] proposed a stochastic matrix factorization method to extract frequency features from noisy spectrograms. However, existing methods still lack computational efficiency and real-time adaptability, especially under complex, non-stationary conditions with multiple noise sources.

This research introduces a novel diagnostic framework to overcome the limitations of conventional techniques, which suffer from high sensitivity to operational parameters and require complex signal processing for interference suppression. Existing methods lack robustness in environments with multivariate random pulse noise, necessitating a more advanced analytical approach. The proposed framework leverages the properties of non-stationary signals under transient noise interference to enhance demodulation robustness and improve band selection accuracy. Central to this study is a Markovian spectral transition model with temporal dependencies, tailored for railway bogie axle bearing diagnosis in non-stationary environments. The methodology integrates Markov transition matrices with wavelet transforms and signal reconstruction, and incorporates a limiting-amplitude interference strategy based on weighted averaging to identify and mitigate transient noise effects. This approach significantly improves conventional Kurtogram methods in identifying characteristic frequency bands for bearing fault detection.

The principal contributions of this research are threefold:

1. Advanced Markovian-Wavelet Integration Framework: A novel signal processing paradigm that mathematically synthesizes Markovian modeling with multi-resolution wavelet analysis, creating a unified theoretical framework for signal decomposition and state characterization. The framework introduces a systematic approach to integrate wavelet coefficients into Markovian state representations.
2. Innovative Amplitude-Adaptive Interference Suppression Mechanism: This mechanism establishes a dynamic threshold for amplitude interference limitation by using the period signal mean as a statistical anchor. It calculates this mean for each period and constructs a weighted threshold to identify interference based on deviations from this baseline, effectively separating noise from fault-related components.
3. Comprehensive Diagnostic Framework: A unified mathematical methodology that formalizes the integration of multiple signal processing techniques, establishing theoretical foundations for parameter optimization and defining systematic relationships between different processing stages. The framework provides a structured approach to combine various signal analysis methods into a cohesive theoretical system.

This study is structured as follows: Section 2 establishes the theoretical foundation. Section 3 details the proposed Markov Latent Frequency Transition Peak Rate with Periodic Mean (MLFTPR-PM) methodology. Section 4 validates the approach through two case studies: Section 4.1 demonstrates its effectiveness through experimental validation using actual bogie axle bearings from a railway locomotive bow-type bogie system, while Sect. 4.2 further extends the application scope to verify its broader validity. Together, these case studies bridge theoretical concepts with practical engineering applications.

2 Preliminaries

This section revisits the key metric for identifying signal transformations. It analyzes three critical aspects: local peak ratios, energy levels, and zero crossing rates. By examining peak ratios, it detects abnormal spikes or dips; analyzing energy levels helps identify strength fluctuations; and assessing zero crossing rates reveals frequency disruptions. Through this integrated approach, the metric effectively detects diverse signal anomalies, proving valuable in applications like mechanical fault diagnosis and medical signal monitoring. Techniques like Short-time Energy (STE) [30], Short-time Kurtosis (STK) [31], and Short-time Zero Crossing Rate (STZCR) [30, 32] are employed for this purpose.

A discrete model represented by a time series $[x_n]$ with indices ranging from 1 to N. To ensure consistent sample weighting across each frame, a rectangular window function denoted as w is applied. The signal analysis is performed utilizing a set of parameters: m denotes the time index, f signifies the frame index, and h corresponds to the extent of the sliding window.

$$x_f[m] = x[m + f \cdot h] \cdot w[m] \tag{1}$$

Samples are identified as local peaks within the sliding window of the signal when they surpass their immediate neighboring values. The criterion for this peak detection can be formalized as follows.

$$\begin{aligned} &x[m] - x[m-1] > 0, \\ &x[m+1] - x[m] \leq 0 \end{aligned} \tag{2}$$

In signal processing, accurately detecting peaks indicating signal changes requires considering both signal magnitude and variation rate. Traditional methods like STE, STK, and STZCR mainly focus on amplitude, which may miss important dynamic components. By introducing a threshold m_d, these limitations can be improved, particularly in noisy conditions. The threshold filters out noise-induced fluctuations, enabling more accurate peak detection. This enhancement allows for precise tracking of signal shifts and better anomaly identification.

$$\begin{aligned} &x[m] - x[m-1] > m_d, \\ &x[m+1] - x[m] \leq m_d \end{aligned} \tag{3}$$

The Short-Term Local Peak Rate (STLPR) is calculated as the proportion of filtered conditional peaks, denoted as N_p, relative to the total number of samples within a moving window. These peaks are identified and counted using a sliding window approach.

$$\text{STLPR} = \frac{N_p}{M} \tag{4}$$

where M denotes the window function's length.

To capture the local characteristics of the signal over the window duration, a metric quantifying anomaly density within a moving window is employed, as described by Eq. 4. This assessment focuses on evaluating peaks to determine the signal's anomaly density.

3 The proposed Markov latent frequency transition peak rate with periodic mean (MLFTPR-PM)

The process of selecting an optimal threshold, denoted as m_d, for identifying conditional peaks is integral to maintaining the precision of Short-Term Local Peak Rate (STLPR). This selection becomes particularly challenging in scenarios characterized by transient non-Gaussian noise, as manual determination of the threshold often leads to inconsistencies, thereby compromising analytical reliability. To address these challenges, this research introduces the Markov latent Frequency Transition Peak Rate with Periodic Mean (MLFTPR-PM). This framework integrates signal pre-processing techniques, Markov modeling to detect state transitions, and interference suppression algorithms, all of which collectively enhance the differentiation of signals amidst complex noise environments. The entire process is depicted in Fig. 1.

3.1 Wavelet analysis and environmental noise suppression

The utilization of the Daubechies Wavelet Transform (DbWT) [33, 34], recognized for its smooth characteristics and superior time-frequency localization properties, further strengthens the analysis. By applying DbWT to a vibration signal $x(t)$, both approximation coefficients, $cA_{j,k}$, and detail coefficients, $cD_{j,k}$, are derived. The decomposition of the signal into these coefficients allows for a granular examination of its components across time and frequency domains. This decomposition process can be represented by a summation over the scaling function $\phi_{j,k}(t)$ and the wavelet function $\psi_{j,k}(t)$, where j designates the scale level and k signifies the wavelet's temporal shift.

$$x = \sum_{k=-\infty}^{+\infty} cA_{j,k}\phi_{j,k}(t) + \sum_{k=-\infty}^{+\infty} cD_{j,k}\psi_{j,k}(t) \tag{5}$$

In the DbWT decomposition, higher-level approximation and detail coefficients are systematically derived from successive stages. Initially, the original signal is decom-

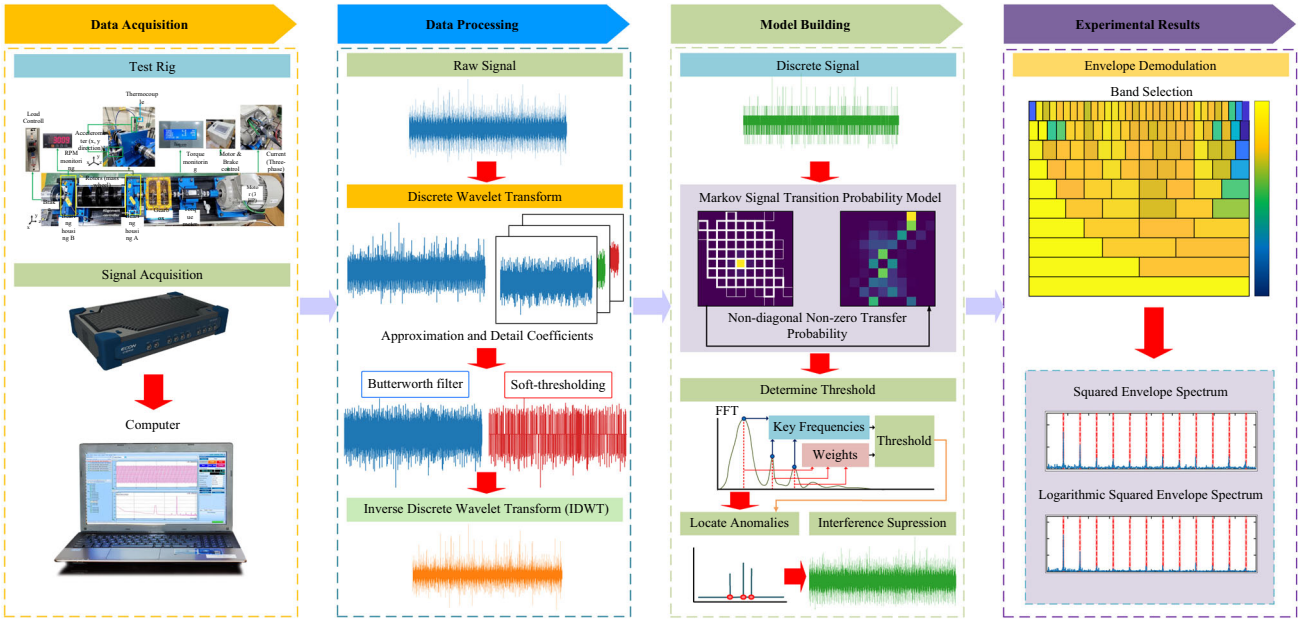

Fig. 1 The framework of the proposed method

posed via wavelet transforms into an approximation and a detail component. The approximation coefficients from one stage become the input for the next, refining these components iteratively. This iterative process effectively preserves and recovers signal features across various frequencies and scales, capturing both macroscopic trends and microscopic nuances. The process continues until the desired level is reached, yielding a hierarchical breakdown ready for further analysis. This procedure can be expressed as follows:

$$\begin{aligned} cA_{j,k} &= \sum_{n} h[n-2k]x_{j-1,n} \\ cD_{j,k} &= \sum_{n} g[n-2k]x_{j-1,n} \end{aligned} \tag{6}$$

where $h[n]$ and $g[n]$ denote the low-pass and high-pass filters respectively, the term $x_{j-1,n}$ corresponds to the lower frequency component of the current approximation stage, embodying the signal's macroscopic trends and long-term behavioral attributes.

For further refinement, the approximation coefficients and detail coefficients are thresholded and filtered. The filtered approximation coefficients, denoted as cA', are obtained by applying a Butterworth filter, which is mathematically described as follows.

$$cA_n^{'} = \sum_{i=0}^{M} b_i \cdot cA_{n-i} - \sum_{j=1}^{N} a_j \cdot cA_{n-j}^{'} \tag{7}$$

For Eq. 7, the feed-forward and feedback coefficients of the filter are denoted by b_i and a_i, respectively. The index j begins at 1 because a_0 is typically normalized to 1.

To reduce noise, soft-thresholding is employed on the detail coefficients (denoted as cD') at each decomposition stage, as illustrated below.

$$cD_i^{'} = \begin{cases} \text{sgn}(cD_i)(|cD_i| - \varepsilon), & |cD_i| \geq \varepsilon \\ 0, & |cD_i| < \varepsilon \end{cases} \tag{8}$$

The threshold value ε is set as a specified percentage (q) of the maximum value of cD_i, as defined by the equation below.

$$\varepsilon = q \cdot \max(cD_i) \tag{9}$$

In wavelet signal processing, the Inverse Discrete Wavelet Transform (IDWT) reconstructs refined signals by synthesizing post-processed approximation and detail coefficients. After noise and disturbance mitigation, IDWT integrates modified coefficients via up-sampling and convolution, preserving critical features while suppressing noise. Mathematically, it combines processed low-frequency and high-frequency coefficients to restore time-domain signals with enhanced fidelity, optimizing clarity for analysis and application. The signal recovery is mathematically represented as follows:

$$\hat{x}(t) = \sum_{j=-\infty}^{\infty} \left(cA_{j,k}^{'} \phi_{j,k}(t) + \sum_{k=-\infty}^{\infty} cD_{j,k}^{'} \psi_{j,k}(t) \right) \tag{10}$$

The scaling function and wavelet function, denoted by $\phi_{j,k}(t)$ and $\psi_{j,k}(t)$ respectively, incorporate scale and shift parameters (j, k). Meanwhile, peaks that significantly deviate from the original signal's mean must be preserved, these peaks are identified by indices satisfying the following condition:

$$\Pi = \left\{ i \mid x_i(t) > \tau \vee x_i(t) < -\tau, i \in \{1, \ldots, |n|\} \right\} \tag{11}$$

where τ denotes the mean of the original signal, the identification of peaks within a reconstructed signal is defined by the following equation.

$$\hat{x}_i^{'}(t) = \begin{cases} x_i(t), & \text{if } i \in \Pi \\ \hat{x}_i(t), & \text{if } i \notin \Pi \end{cases} \tag{12}$$

To ensure the reproducibility and robustness of the proposed methodology, the key signal processing parameters were selected based on established defaults and standard practices within the field of vibration analysis, rather than through dataset-specific optimization. The specific choices are detailed as follows: the Daubechies 4 (db4) wavelet was employed as the wavelet basis for the DbWT over 3 decomposition levels, with symmetric padding used for boundary handling. A 2nd-order Butterworth filter was applied for low-pass filtering, and a rectangular window was used for framing the signal. The soft-thresholding parameter q was set to 0.1. This commitment to using standard parameters ensures that the presented results are derived from a consistent and transparent framework, facilitating independent verification.

3.2 Markov chain analysis and signal state transition modeling

In the field of signal processing and stochastic systems analysis, the implementation of Markov chain modeling presents an approach to characterizing state transitions within reconstructed signals. This mathematical framework provides a robust foundation for analyzing complex systems through the lens of probabilistic state transitions, wherein the system's evolution is governed by well-defined statistical principles. The fundamental premise of Markov chain analysis rests upon the distinctive Markov property, which posits that the future state of a system is conditionally independent of its historical trajectory, being influenced solely by its current state. This concept can be formally expressed through the following probabilistic relationship:

$$P(x_i \mid x_{i-1}, x_{i-2}, ..., x_1) = P(x_i \mid x_{i-1}) \tag{13}$$

where x_i, designated as the next state, is entirely determined by the probability associated with the current state x_{i-1}, this implies that the state transition probability relies solely on the immediate previous state, disregarding all earlier states in the sequence.

Within the framework of Markov chains, the Markov property defines a system where each state transition is probabilistic, with the current state depending exclusively on the immediate prior state. This property signifies that future states are conditionally independent of past states when the present state is known. Formally described by a transition probability matrix, the system's transition behavior enumerates conditional probabilities for all possible state pairs. For a system with n states, this matrix provides a holistic representation of n^2 potential state transitions, constructed through a specialized computational approach. Specifically, the matrix structure is as follows:

$$M_{TPM} = \begin{bmatrix} p_{11} & p_{12} & \cdots & p_{1j} & \cdots \\ p_{21} & p_{22} & \cdots & p_{1j} & \cdots \\ \vdots & \vdots & & \vdots & \\ p_{i1} & p_{i2} & \cdots & p_{ij} & \cdots \\ \vdots & \vdots & \vdots & \vdots & \end{bmatrix} \tag{14}$$

3.3 Signal state mapping and transition frequency calculation

By integrating wavelet reconstruction, the method transforms signal amplitudes into indexed intervals—denoted as I—thereby facilitating the identification of signal states. This approach converts complex continuous signals into a discrete format, as specified in Eq. 15, enabling effective differentiation between normal states and anomalies while maintaining the integrity of state transitions. The conversion of amplitudes to interval indices is governed by the following equation:

$$S_i = \begin{cases} j, & x_n[i] \in S_j \\ j, & x_n[i] = \max(x_n),\ j = n_{\text{bin}} - 1 \end{cases} \tag{15}$$

To map the signal onto the state space S_j of the Markov model, its amplitude is partitioned into 10 bins ($n_{\text{bin}} = 10$). This specific value falls within a range validated by previous studies [3, 28], where the sensitivity of the final detection threshold to the bin count is negligible.

$$\begin{aligned} S_j &= [\min(x_n) + (j-1) \cdot \Delta, \min(x_n) + j \cdot \Delta] \\ \Delta &= \frac{\max(x_n) - \min(x_n)}{n_{\text{bin}}} \end{aligned} \tag{16}$$

The granularity of the discrete state representation in the Markov model analysis is defined by n_{bin}, while Δ represents the consistent gap used for signal discretization.

The Markov Transition Matrix (MTM), denoted as N_{ij}^{MTM}, facilitates this process by mapping out the frequencies of

state transitions, which is a common step in analyzing state sequences using statistical methods.

$$N_{ij}^{MTM} = \sum_{n=1}^{n_s-1} \delta(S_n = i, S_{n+1} = j) \tag{17}$$

where the Kronecker Delta function, $\delta(x, y)$, returns 1 if x and y are identical, and 0 otherwise. n_s represents the total number of states in the sequence S.

To determine a typical percentage threshold for the baseline of a frequency distribution, one must compute the aggregate of all elements within the matrix. The computation is carried out using the following expression:

$$\theta = \alpha \cdot \sum_{i=1}^{n} \sum_{j=1}^{n} N_{ij}^{MTM} \tag{18}$$

where the variable α, configured as 0.1, denotes the ratio of normal transition occurrences to the total frequency. This specific value is chosen as a conservative threshold to effectively filter out the high-frequency transitions concentrated along the diagonal of the transition matrix, while preserving the rare, off-diagonal transitions that are indicative of anomalies.

Setting the values of diagonal entries and their immediate neighbors that exceed a specified threshold θ to zero nullifies routine transitions within the matrix. This modification results in a matrix that highlights only significant transitions. The detailed procedure is as follows:

$$N_{ij}^{MTM'} = \begin{cases} 0, & \text{if } i = j \\ 0, & \text{if } N_{ij}^{MTM} > \theta \\ N_{ij}^{MTM}, & \text{if } i \neq j \text{ and } N_{ij}^{MTM} \leqslant \theta \end{cases} \tag{19}$$

After eliminating the normal elements, normalization of the state matrix results in the formation of the Markov Transition Probability Matrix (MTPM), denoted as P_{ij}. This matrix reflects the probability of transitioning from state i to state j. The formula for P_{ij} is as follows:

$$P_{ij} = \frac{N_{ij}^{MTM'}}{\sum_{j=1}^{N} N_{ij}^{MTM'} - \left(1 + N_{ij}^{\theta}\right)} \tag{20}$$

where the count of standard transitions in row i that exceed the predefined threshold θ is indicated by N_{ij}^{θ}.

Due to rigidity from insufficient anomalous fragments, it is critical to consider the amplitude and frequency features of the time series. First, calculate the maximum amplitude of each frequency component, then its mean value, select the top-k frequencies with the highest amplitudes, and finally compute their corresponding periods. This approach accurately captures the signal's periodic traits, enabling effective time series replacement while preserving the original signal's fundamental characteristics. The detailed computation process is as follows.

$$p_i = \lceil \frac{T}{f_i} \rceil \text{ where } \{f_1, \ldots, f_k\} = \arg_{f_* \in \{1, \ldots, \lfloor \frac{T}{2} \rfloor\}} \text{Topk}(\text{Avg}(|\text{FFT}(\hat{x}_t)|)) \tag{21}$$

where $\text{Topk}(\text{Avg}(|\text{FFT}(\hat{x}_t)|)) = \{f_1, ..., f_k\}$ represents the top k frequency components selected from the averaged frequency amplitudes obtained through Fast Fourier Transform (FFT) analysis (these f_i are the high-amplitude frequency components used in Eq. 21). T denotes the total time length (or total number of sampling periods) of the reconstructed signal $\hat{x}_t$, providing a time-scale benchmark for calculating the period p_i of each selected frequency component f_i.

Following the key periods p_i extracted in Eq. 21, it is critical to filter valid sampling points within each period to ensure the accuracy of subsequent periodic mean calculations. Since real vibration signals may contain local missing values or transient noise interference, using all sampling points directly would cause mean deviation. Thus, an index set of valid sampling points is established to exclude invalid data:

$$C_i(t) = \left\{ (t - j) \mod L \mid j = 0, 1, 2, \ldots, \left\lfloor \frac{T}{p_i} \right\rfloor \right\} \text{ such that} [(t - j) \mod L]_{\text{missing}} = 0 \tag{22}$$

where $C_i(t)$ denotes the set of valid indices for time t within period p_i, $(t-j) \mod L$ represents indices offset by j steps from t (with L being the total number of samples), and $[(t-j) \mod N]_{\text{missing}} = 0$ indicates that the corresponding sampling values are non-missing.

The next step is to quantify the baseline signal level for each period. This baseline, represented as $\bar{x}_{p_i}$ and reflected by the periodic mean, serves as a core input for calculating the weighted periodic threshold. Its calculation method is as follows:

$$\bar{x}_{p_i} = \frac{1}{|C_i(t)|} \sum_{j \in C_i(t)} \hat{x}(j) \tag{23}$$

To integrate the baseline signal levels $\bar{x}_{p_i}$ of different periods into a unified weighted periodic threshold, it is first necessary to determine the weight coefficient w_i for each period p_i. Mathematically, this weight is defined as the quotient of the amplitude of the i^{th} frequency component (corresponding to period p_i) divided by the total sum of the amplitudes of all selected key frequencies. This calculation method normalizes the weights, ensuring their sum equals

exactly 1—a crucial step that lays a solid foundation for subsequent weighted average computations. It guarantees each frequency's contribution to the final threshold is proportional to its relative amplitude, which in turn enhances the accuracy and reliability of the threshold by aligning weight distribution with the signal's intrinsic energy characteristics. The specific formula for w_i is provided in Eq. 24.

$$w_i = \frac{Amp(f_i)}{\sum_{i=1}^{k} Amp(f_j)}, \quad i \in \{1, 2, \ldots, k\} \tag{24}$$

where $Amp(f_i)$ denotes the amplitude calculation operator.

With the periodic means $\bar{x}_{p_i}$ and their corresponding weights w_i determined, the calculation formula for the weighted periodic threshold τ_{markov} is as follows:

$$\tau_{\text{markov}} = \sum_{i=1}^{k} w_i \cdot \bar{x}_{p_i} \tag{25}$$

Therefore, the STCLPR mentioned in 4 can be improved to the following MLFTPR-PM:

$$MLFTPR - PM = \frac{1}{M} \sum_{n=0}^{M-2} \mathbb{1}\{\tau_{\text{markov}} > \Delta x[n]\} \cdot \mathbb{1}\{\tau_{\text{markov}} > \Delta x[n+1]\} \tag{26}$$

The indicator function, denoted here by $\mathbb{1}$, acts as a binary switch based on the positivity of its input, assigning 1 if the argument is positive and 0 otherwise. $\Delta x[n]$ represents the absolute difference between the signal x and its next sample point.

To enhance signal reliability and analytical effectiveness while preserving the essential characteristics of the original signal, a thorough analysis of the MLFTPR-PM across the entire signal is conducted. The goal is to compute an average value that serves as a detection threshold for pinpointing irregular boundaries and establishing a robust window to capture any overlooked anomalies. Subsequently, corresponding segments in the underlying signal are adjusted to manage amplitude peaks, thereby mitigating anomaly impacts. The methods employed are encapsulated in the following equations:

$$\lambda = \frac{1}{K} \sum_{k=0}^{K-1} MLFTPR - PM[k] \tag{27}$$

$$\Omega = \left\{k \mid MLFTPR - PM[k] > \gamma \cdot \lambda\right\} \tag{28}$$

where Ω defining anomaly boundaries, γ as the average coefficient.

The final predicted value is derived through the aggregation of weighted averages calculated across every single period:

$$y_{lim}^{i} = \sum_{i=1}^{k} w_i \cdot \frac{1}{|C_i(t)|} \sum_{j \in C_i(t)} \hat{x}_t[j], \quad i \in (k \cdot M, k \cdot M + h), \forall k \in \Omega \tag{29}$$

This methodological framework has two key functions. First, it effectively reduces anomaly-induced distortions—filtering out noise from anomalies to boost signal clarity and reliability. Second, it preserves the signal's basic characteristics, which hold critical information for accurate analysis. Mathematical precision in this method is vital for reliable signal reconstruction. Advanced algorithms process signal data to reconstruct it close to its original form (even with noise) while maintaining key temporal patterns (trends, periodicity, dependencies) in time series—essential for predictions and informed decisions.

4 Experiment validation

4.1 Case study I

4.1.1 Experimental apparatus and data acquisition

To rigorously assess the efficacy and robustness of the proposed methodological framework, a comprehensive real-world testing facility was established using actual railway components and operational conditions. The testing facility utilized genuine bogie axle bearing systems from a CRH380B high-speed train, as shown in Fig. 2. This real-world testing environment was specifically designed to capture authentic operational conditions and collect comprehensive vibration datasets from actual bogie axle bearing systems in service conditions.

The testing facility incorporated an authentic bogie axle pair with a precise diameter of 2500 mm, matching the exact specifications used in operational high-speed trains. This specific dimension was selected to maintain complete authenticity with in-service equipment, as it directly influences the mechanical response characteristics and vibration patterns observed during actual railway operations. The use of production-specification components ensures that all test data accurately reflects the true performance characteristics encountered in regular service conditions. Fig. 3 provides a detailed technical illustration of the actual testing facility, documenting the physical layout, component integration, and sensor deployment configuration. This technical documentation precisely maps the structural configuration, operational parameters, and sensor placement strategy used to monitor

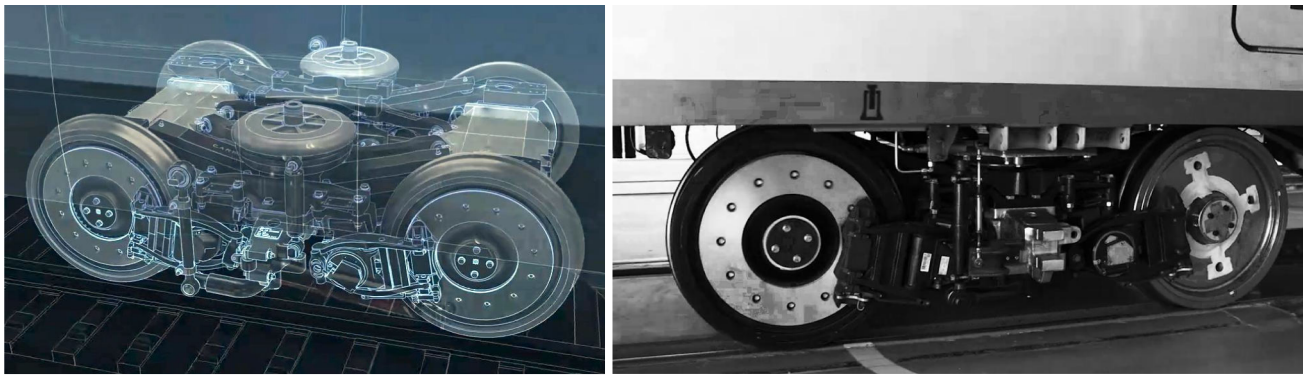

(a) (b)

Fig. 2 **a** Technical diagram of the actual railway locomotive bow-type bogie system; **b** Photograph of the operational railway locomotive bogie assembly installed on a high-speed train

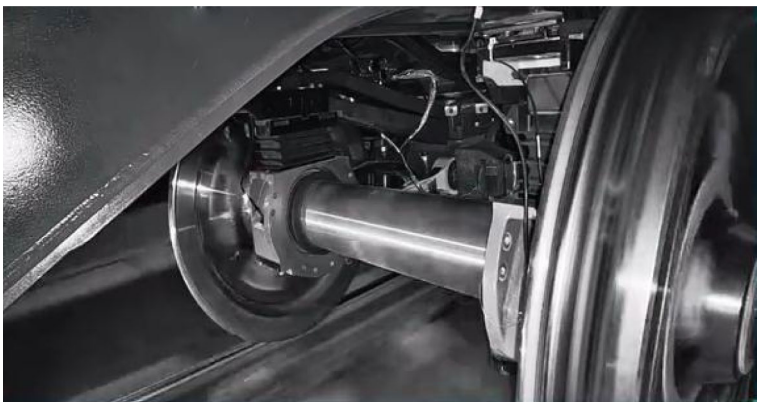

(a)

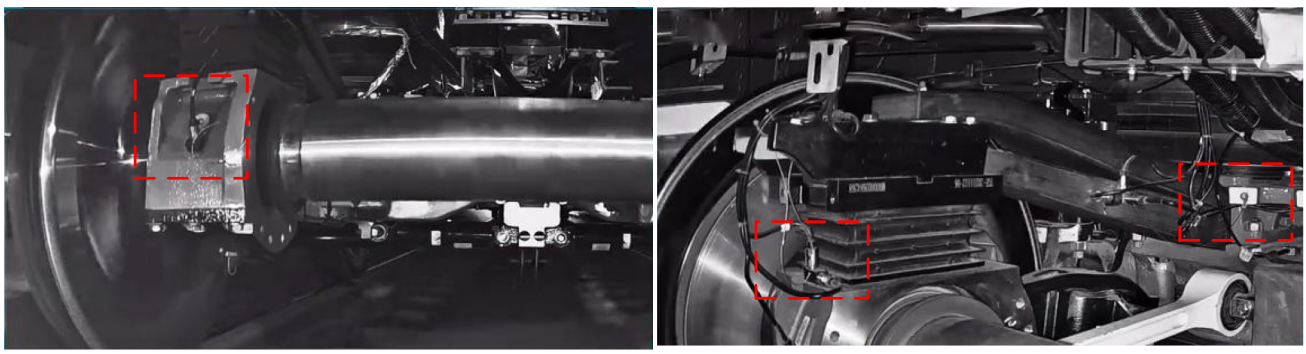

(b) (c)

Fig. 3 **a** Actual bogie axle bearing configuration from the railway locomotive; **b** and **c** Diagram illustrating the placement and orientation of acceleration sensors on the bearing system

real-time vibration signals from the operational bearing system. The testing facility's design emphasizes the use of actual railway components and authentic operating conditions to ensure direct applicability of the validation results to real-world scenarios.

The bearing's geometric configuration was characterized by several precisely determined parameters, each of which plays a crucial role in the overall dynamic behavior of the system. Specifically, the rolling element diameter (d) was established at 26.9 mm, while the pitch circle diameter (D) was configured to 180 mm. Furthermore, the contact angle (θ) was maintained at 9 degrees, a parameter that significantly influences the load distribution patterns and tribological interactions within the bearing assembly. The bearing configuration included 19 balls (N), which constitute the primary load-bearing elements and contribute signifi-

cantly to the generation of characteristic vibration signatures during both nominal and anomalous operating conditions.

Under the prescribed experimental conditions, detailed frequency analysis revealed specific characteristic frequencies that serve as fundamental indicators of bearing performance. The ball pass frequency for the inner race (BPFI) was experimentally determined to be 8.36 Hz, whereas the ball pass frequency for the outer race (BPFO) was established at 7.936 Hz. These frequencies represent critical diagnostic parameters that serve as baseline references for the identification and characterization of potential bearing anomalies. The precise determination of these frequencies was accomplished through the implementation of state-of-the-art sensing technologies coupled with sophisticated data acquisition methodologies.

To ensure comprehensive signal capture and analysis capabilities, the vibration signal acquisition was conducted at a sampling frequency of 10000 Hz. This elevated sampling rate was strategically selected to guarantee the capture of all pertinent frequency components within the vibration spectrum, thereby enabling the detection and analysis of high-frequency phenomena and transient events that might be imperceptible at lower sampling frequencies. This high-fidelity data acquisition approach facilitates a more nuanced understanding of the bearing's dynamic behavior and enhances the capability for precise fault diagnosis.

The experimental protocol was executed with meticulous attention to methodological rigor and data quality assurance. A sophisticated array of sensors was strategically deployed around the bearing assembly to capture multi-directional vibration signatures, thereby providing a comprehensive three-dimensional characterization of the bearing's dynamic state. Prior to experimental trials, all sensing elements underwent rigorous calibration procedures to ensure measurement accuracy and data reliability. Throughout the experimental campaign, the bearing system was subjected to a diverse range of operating parameters, including variations in rotational velocity and applied loads, to simulate the broad spectrum of conditions encountered during actual service operations. This systematic approach to experimental design and data collection resulted in the generation of a comprehensive and statistically significant dataset, enabling robust evaluation of the proposed methodology across diverse operational scenarios.

4.1.2 Experimental validation and comparative analysis

This study employs the Discrete Wavelet Transform (DWT) [33] as a pre-processing methodology for signal decomposition, as illustrated in Fig. 4. The implementation of DWT facilitates the systematic decomposition of complex vibration signals into their fundamental components, enabling comprehensive analytical examination. DWT maintains signal fidelity through the preservation of intrinsic signal dynamics. The technique effectively processes both long-term trends and transient fluctuations within vibration signals, maintaining the integrity of critical characteristics including frequency content and amplitude variations. This preservation is particularly significant for signals subject to stochastic transient perturbations that may obscure underlying signal characteristics. Analysis of level 1 approximation coefficients, presented in Fig. 4 (b), reveals the fundamental signal characteristics. These coefficients constitute a low-frequency representation of the original signal, demonstrating the effective separation of low-frequency components from high-frequency noise and transient elements. This decomposition is essential for understanding the system's fundamental behavioral characteristics. The level 1, 2, and 3 detail coefficients, illustrated in Fig. 4(c)-(e), provide quantitative representation of high-frequency content. These coefficients elucidate rapid variations and localized features within the signal, potentially corresponding to stochastic transient disturbances. Analytical examination of these coefficients enables the quantification of disturbance characteristics, including amplitude, frequency, and temporal duration, facilitating enhanced signal analysis, noise reduction, and anomaly detection methodologies.

As a result, the long term stability attributes of the signal are more conspicuously accentuated, and small scale interferences are efficiently suppressed, as demonstrated in Fig. 5 (a) and (b). In Fig. 5(c), a comparative analysis between the original and the reconstructed signals is presented. The reconstructed signal not only successfully mitigates noise but also accentuates significant external interferences. This dual effect enhances the clarity of anomalous transitions within the signal, making it easier to identify and analyze deviations from the normal signal pattern. By highlighting critical information, this approach substantially improves the accuracy of anomaly detection. Subsequently, the signal is partitioned into distinct states in accordance with Eq. (16)-(20). As depicted in Fig. 5(d), this segmentation gives rise to discrete signals that exhibit well defined interval distributions under both normal and noisy conditions. This discrete representation simplifies the analysis of the signal, enabling more efficient identification of patterns and anomalies. It also provides a basis for further statistical analysis and modeling of the signal's behavior, facilitating a more comprehensive understanding of the underlying system.

Examination of high-frequency components at each decomposition level demonstrates their capacity to capture rapid signal fluctuations, which serve as indicators of significant behavioral transitions. Conversely, low-frequency components reveal the fundamental structure and temporal evolution of the signal, representing the underlying systematic behavior. The optimization of these coefficients through low-pass filtering and threshold processing enhances

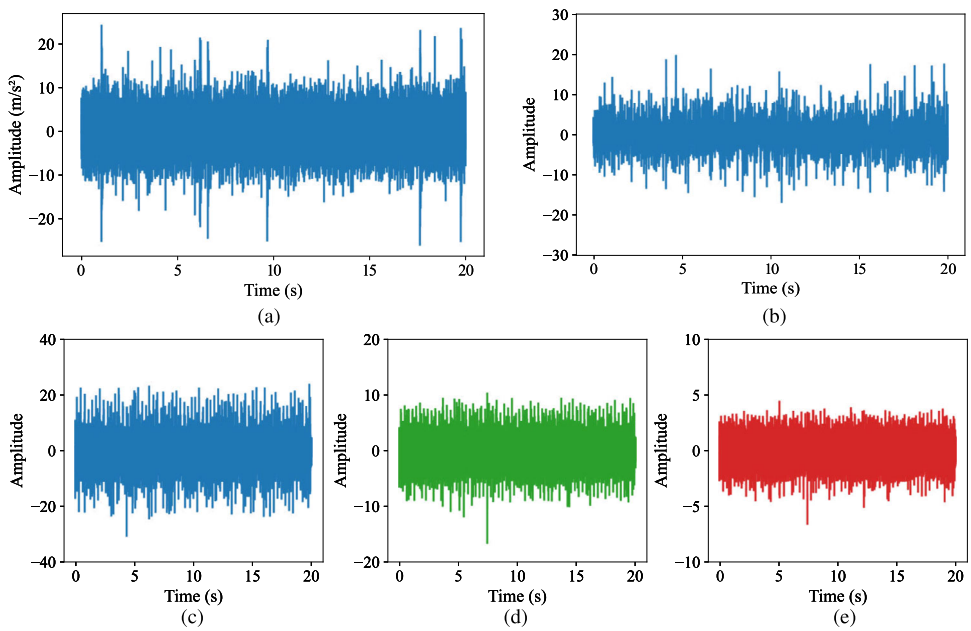

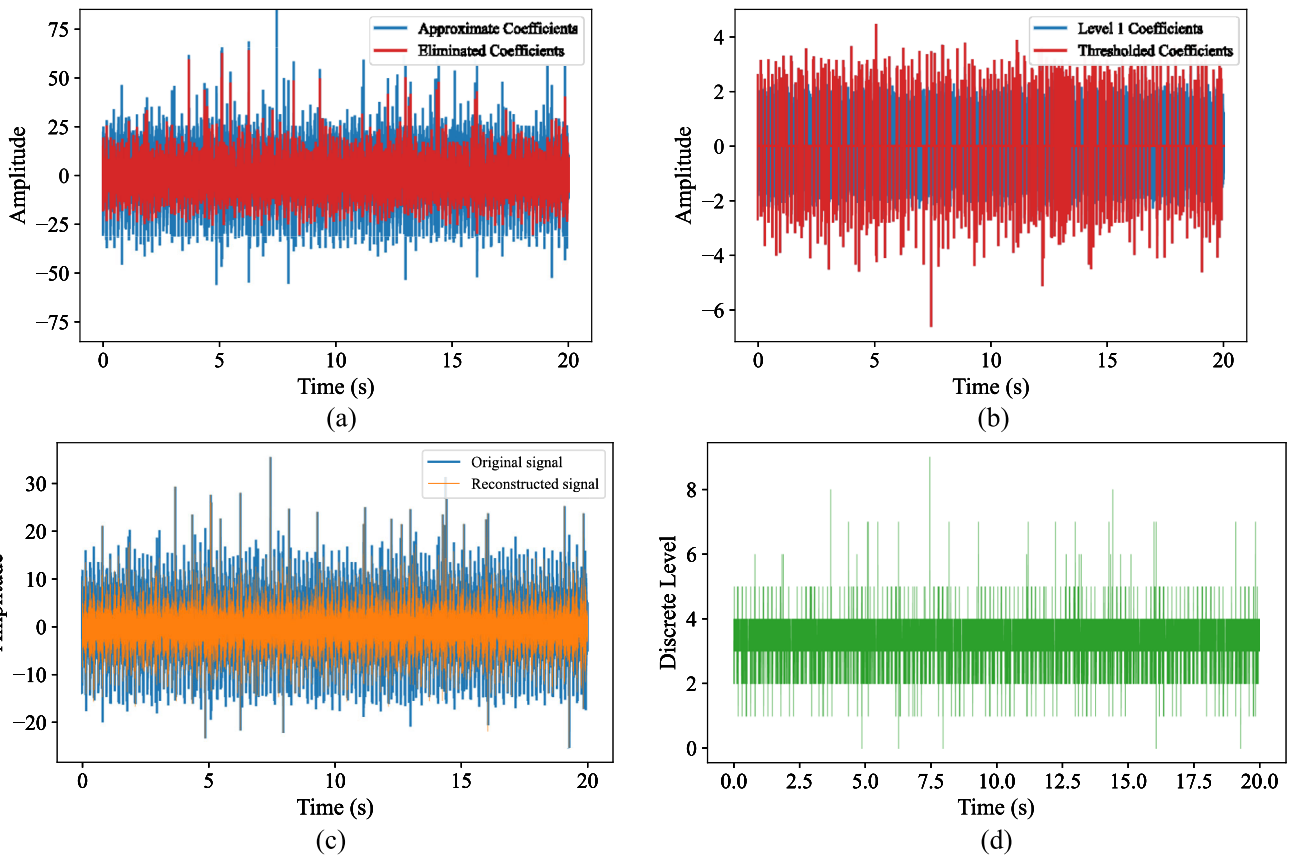

Fig. 4 **a** Raw signal, **b** Level 1 approximation coefficient, **c** Detail coefficient (level 1), **d** Detail coefficient (level 2), and **e** Detail coefficient (level 3) in DWT

Fig. 5 **a** Low-pass filtered approximation, **b** Thresholded detail coefficients, **c** Equidistant signal discretization, **d** Raw and reconstructed Signals

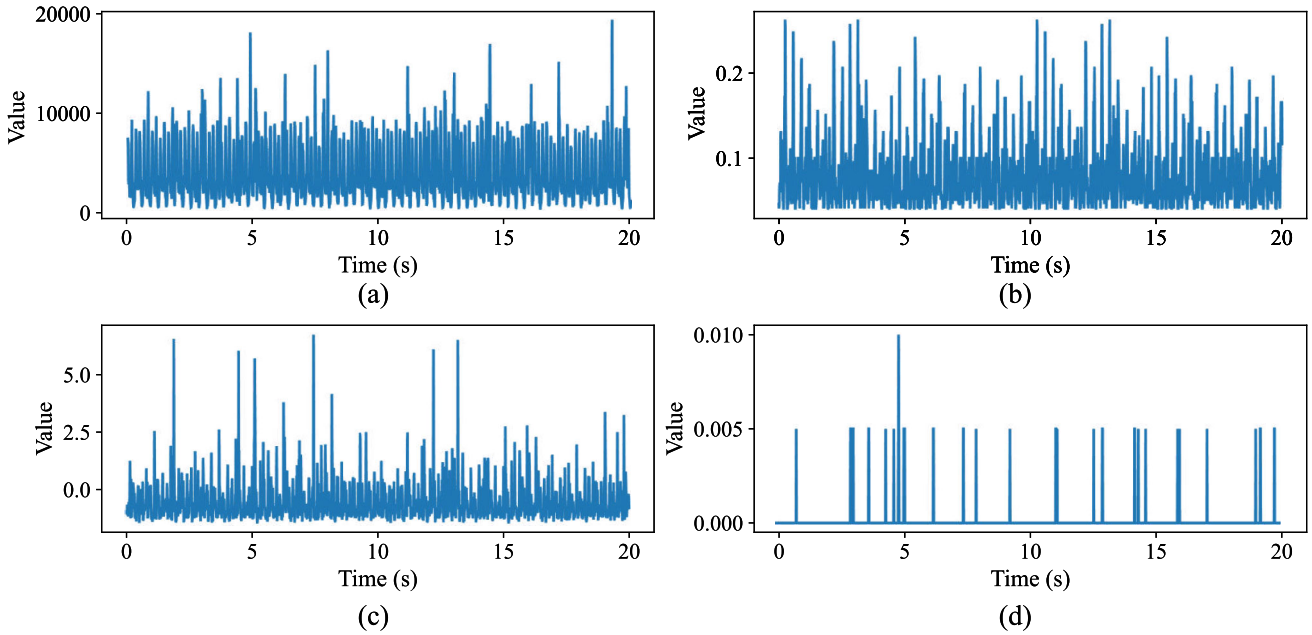

Fig. 6 **a** STE, **b** STZCR, **c** STK, and **d** MLFTPR-PM

signal clarity. Low-pass filtering enables selective attenuation of high-frequency components, while threshold processing facilitates the differentiation of significant features from noise through predetermined threshold values. This methodology effectively eliminates minor perturbations, reduces noise-induced artifacts, and reduces signal complexity while maintaining essential characteristics. Fig. 5(a) and (b) demonstrate the enhancement of long-term stability characteristics and suppression of small-scale interference. Fig. 5(c) presents a comparative analysis between original and reconstructed signals, illustrating effective noise mitigation while preserving significant external interference patterns. This optimization enhances the identification of anomalous transitions, thereby improving detection accuracy. The signal undergoes state-based partitioning according to Eq. (16)-(20). Fig. 5(d) illustrates the resultant discrete signals, characterized by distinct interval distributions under normal and noise-affected conditions. This discretization facilitates efficient pattern recognition and anomaly detection while providing a foundation for statistical analysis and system behavior modeling.

To evaluate the effectiveness of the proposed method in monitoring signal transitions, its performance was compared against several established techniques: Short-Time Energy (STE), Short-Time Kurtosis (STK), and Short-Time Zero Crossing Rate (STZCR). This comparison is illustrated in Fig. 6(a)–(d).

Quantitative evaluation of the STE methodology, as depicted in Fig. 6(a), reveals its capability to detect multiple interference components, though the method exhibits inherent constraints in achieving complete detection coverage across the full spectrum of interference patterns. This is because the STE, based on short time energy calculation, may not be sensitive enough to minor interference. The STZCR approach, depicted in Fig. 6(b), has limitations in differentiating transient noise interferences. Relying on zero crossing rates, it can misinterpret signal variations in complex, non stationary noise environments. The STK method, shown in Fig. 6(c), also struggles to recognize interference components. Being highly sensitive to unaccounted signal noise, it can produce distorted results when non Gaussian noise is present. In contrast, the proposed MLFTPR-PM, as illustrated in Fig. 6(d), excels in accurately detecting all transient noise disturbances. Using Markov modeling and frequency transition analysis, it is robust against other signal aberrations, focusing on latent frequency transitions and peak rates for reliable detection in complex signals.

Fig. 8 presents a visual representation of the frequency and probability distributions of Markov signals through dual heatmaps, facilitating a comprehensive and intuitive understanding of the signal's characteristics. Specifically, the heatmap of Markov signal frequencies in Fig. 8(a) is utilized to uncover the periodicity inherent in state transitions. In this heatmap, the cells along the diagonal with intense coloring indicate a strong tendency for states to persist. This persistence implies the system's resilience and a certain degree of predictability in the signals. The bright spots off the diagonal represent state transitions. These transitions not only reflect the signal's dynamism but also serve as potential indicators of significant events or anomalies within the system. The dark

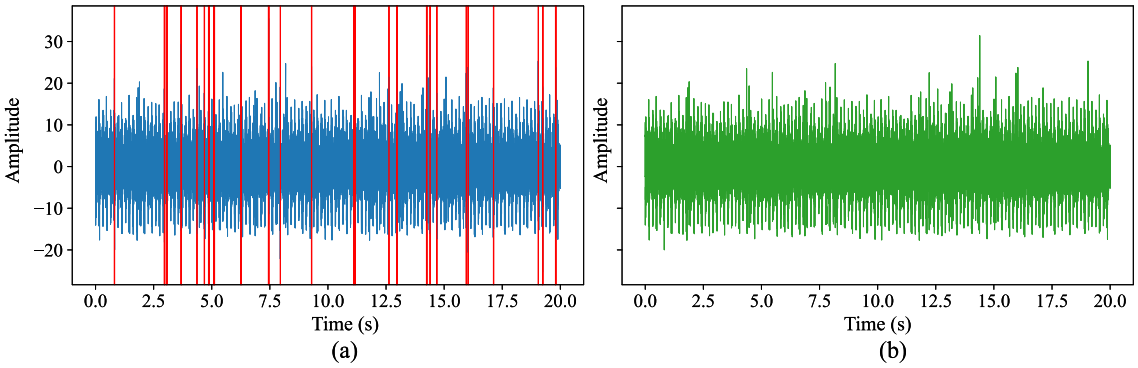

Fig. 7 **a** Signals with interference, **b** Vibration signal with interference suppression

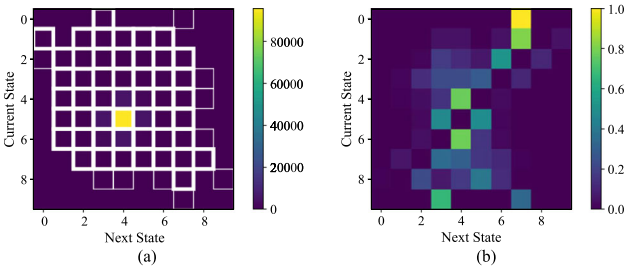

Fig. 8 **a** Markov signal frequencies heat-map, **b** Scaled Markov signal probability heat-map

zones outlined in white represent rare or anomalous transitions, and the thickness of these white borders is proportional to the rarity of these occurrences.

To further analyze the signal and extract more meaningful information, the heatmap is modified. By excluding high frequency self transitions on the diagonal and reducing off diagonal high frequency transitions, a normalized transition probability matrix is generated, as shown in Fig. 8(b). This modification emphasizes lower frequency transitions, effectively expanding the dynamic range of the matrix. Consequently, the refined heatmap becomes a more sensitive means for detecting subtle changes or transition patterns that may have been overlooked in the original frequency matrix.

When the information presented in Fig. 5(d) and Fig. 8(b) is integrated, a series of potential anomaly points can be identified. By applying the formula in Eq. (25), the actual anomaly points can be precisely determined. This combined approach enables a more accurate and comprehensive analysis of the Markov signals, enhancing the ability to detect and understand anomalies in the system under study.

As previously detailed, the proposed MLFTPR-PM metric effectively identifies irregularities related to external transient noises. It shows strong robustness against such disruptions, demonstrating the vibration signal's resilience to external transient impacts. The inclusion of an amplitude limiting component reduces potential amplitude interferences, improving fault identification accuracy.

The ability of this mechanism to control disturbance amplitudes is clearly presented in Fig. 7(a) and Fig. 7(b). By analyzing the states in the transition matrix and the discretized signal, the moment before anomaly occurrence can be estimated. Based on the original signal's position and amplitude, the threshold τ_{markov} is determined to distinguish normal and anomalous behavior in low probability transitions.

In the comparative case study, the Kurtogram [20] and Infogram [35] are used as benchmark techniques. The analysis focuses on a raw bearing vibration signal, which is prone to external transient noise interference. Various methods are applied to mitigate post interference effects and limit amplitude interference in this signal. After post processing, the signals are analyzed via demodulation band selection and envelope analysis.

The outcomes of the demodulation band selection process for the original vibration signal are presented in Fig. 9(a), Fig. 10(a) and Fig. 11(a). To delve deeper into the signal characteristics, additional analyses were conducted using the Squared Envelope Spectrum (SES) [20] and Logarithmic Envelope Spectrum (LES) [35]. The results of these analyses are depicted in Fig. 9(b), Fig. 9(c), Fig. 10(b), Fig. 10(c), Fig. 11(b) and Fig. 11(c).

The Kurtogram method identified a filtered central frequency and bandwidth of [11800Hz, 400Hz]. In contrast, the Infogram method yielded a distinct set of values, with a central frequency and bandwidth of [1400Hz, 400Hz]. Besides, the Autogram method generated yet another set of results, with a central frequency and bandwidth of [2666.6667Hz, 1066.6667Hz].

A meticulous examination of the envelope spectra, as depicted in Fig. 9(b), Fig. 10(b), and Fig. 11(b), reveals a significant discrepancy. Specifically, the characteristic bearing frequency, which, based on theoretical predictions, should be identified as $f_i = 8.36$ Hz, is conspicuously absent. This deviation from the expected results warrants further investigation, as it challenges the conventional understanding of the relationship between the signal processing methods and the

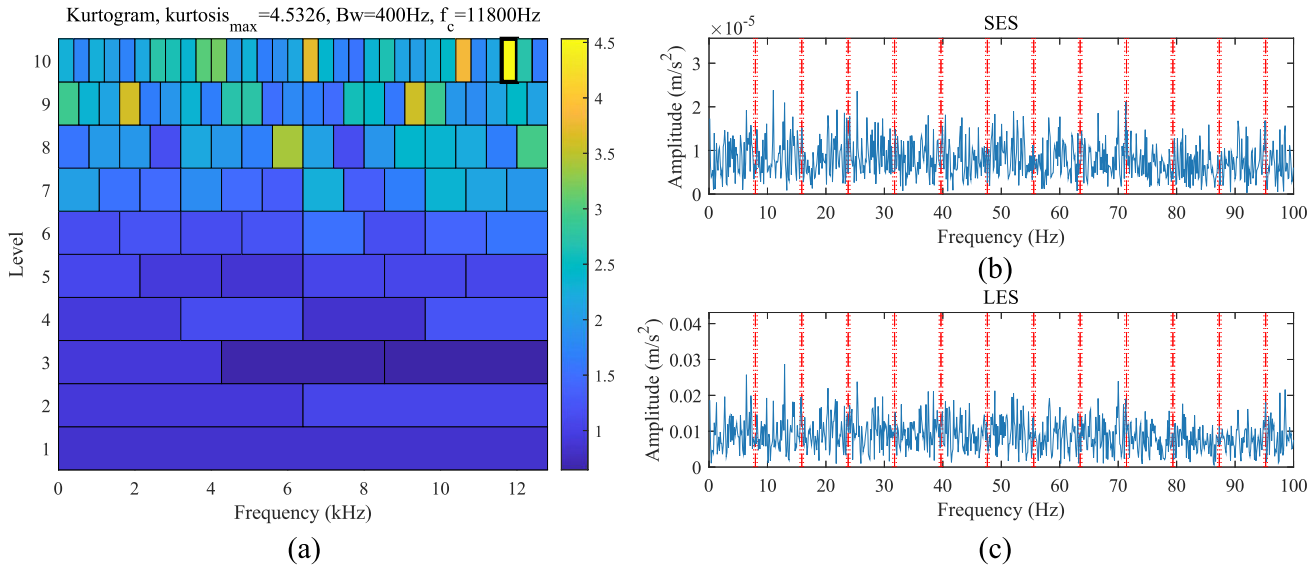

Fig. 9 Raw signal affected by external transient noise interference: **a** Demodulation band determination via beta-Kurtogram, **b** Squared envelope spectrum, **c** Envelope spectrum in logarithmic scale

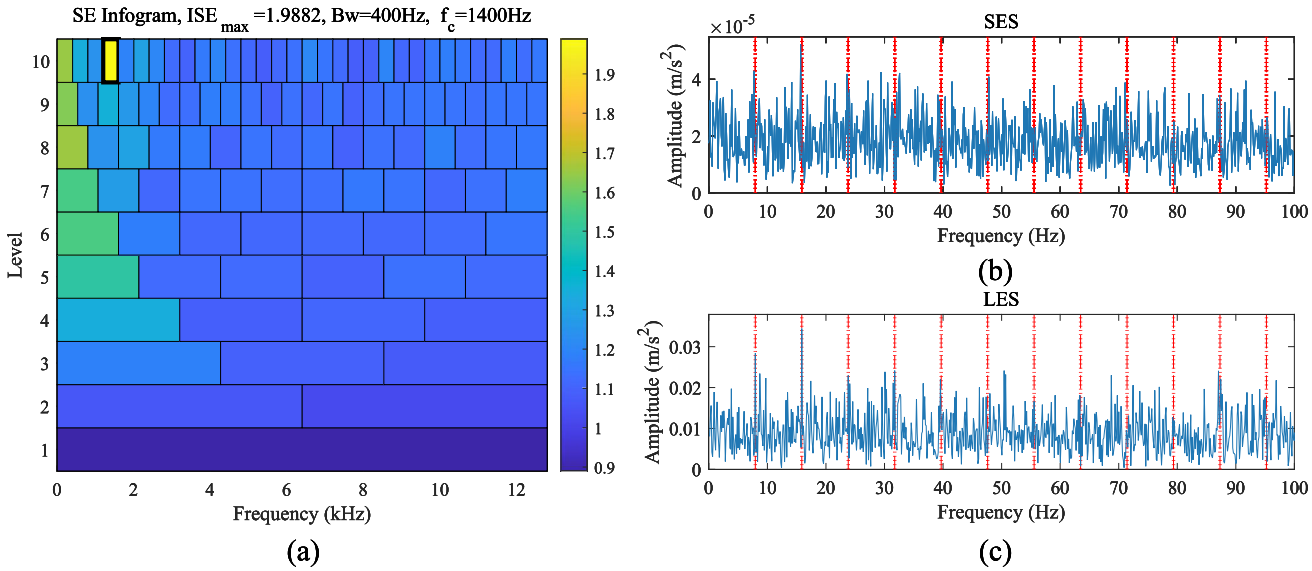

Fig. 10 Raw signal affected by external transient noise interference: **a** Demodulation band determination via Infogram, **b** Squared envelope spectrum, **c** Envelope spectrum in logarithmic scale

identification of bearing related frequencies in this specific context. The diverse results obtained from the Kurtogram, Infogram, and Autogram methods, especially the absence of the characteristic bearing frequency, suggest potential limitations or overlooked factors in the existing signal processing and frequency identification techniques.

Fig. 12(a), Fig. 13(a) and Fig. 14(a) illustrate the impacts of choosing different demodulation bands and performing envelope analysis on signals subsequent to amplitude interference limitation [3] and interference suppression. In contrast, Fig. 12(b), Fig. 12(c), Fig. 13(b), Fig. 13(c), Fig. 14(b) and Fig. 14(c) showcase the envelope analyses carried out using the SES and LES methods. The calculated parameters for the filtered central frequency and bandwidth are [800Hz, 533.3333Hz] for the first set, [6400Hz, 12800Hz] for the second set and [1600Hz, 1066.6667Hz] for the third set.

A comprehensive examination of the envelope analysis results, as presented in Fig. 12(b), Fig. 12(c), Fig. 13(b), Fig. 13(c), Fig. 14(b) and Fig. 14(c), reveals a distinct identification of characteristic frequencies, including f_i, $2f_i$, and $3f_i$. These findings play a pivotal role in validating the efficacy of

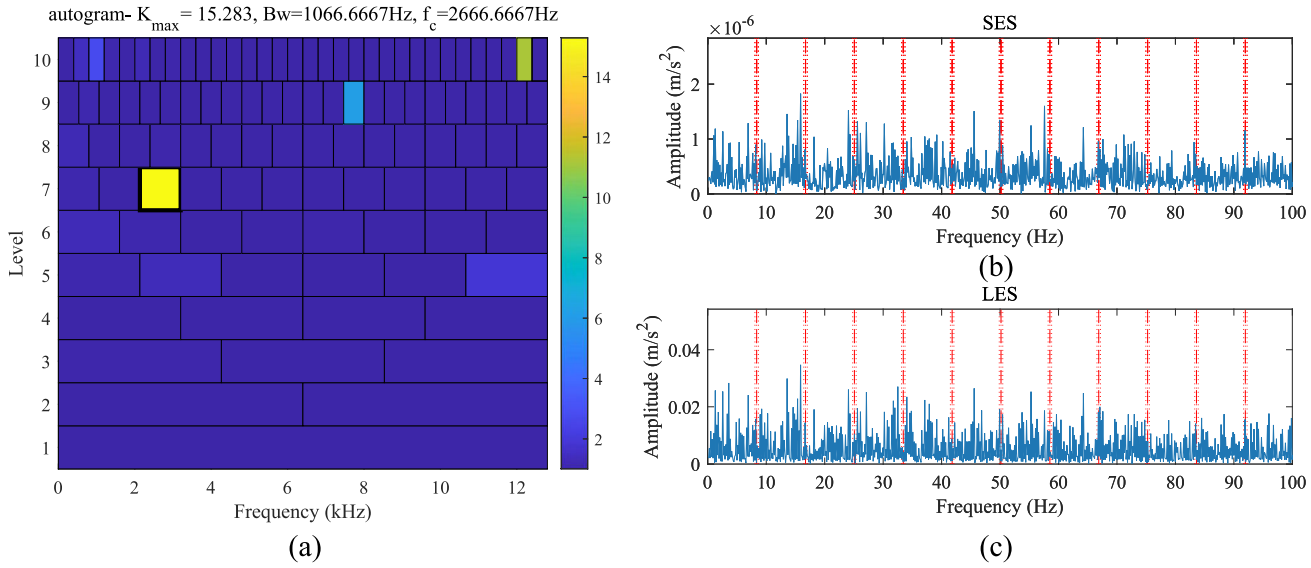

Fig. 11 Raw signal affected by external transient noise interference: **a** Demodulation band determination via Autogram, **b** Squared envelope spectrum, **c** Envelope spectrum in logarithmic scale

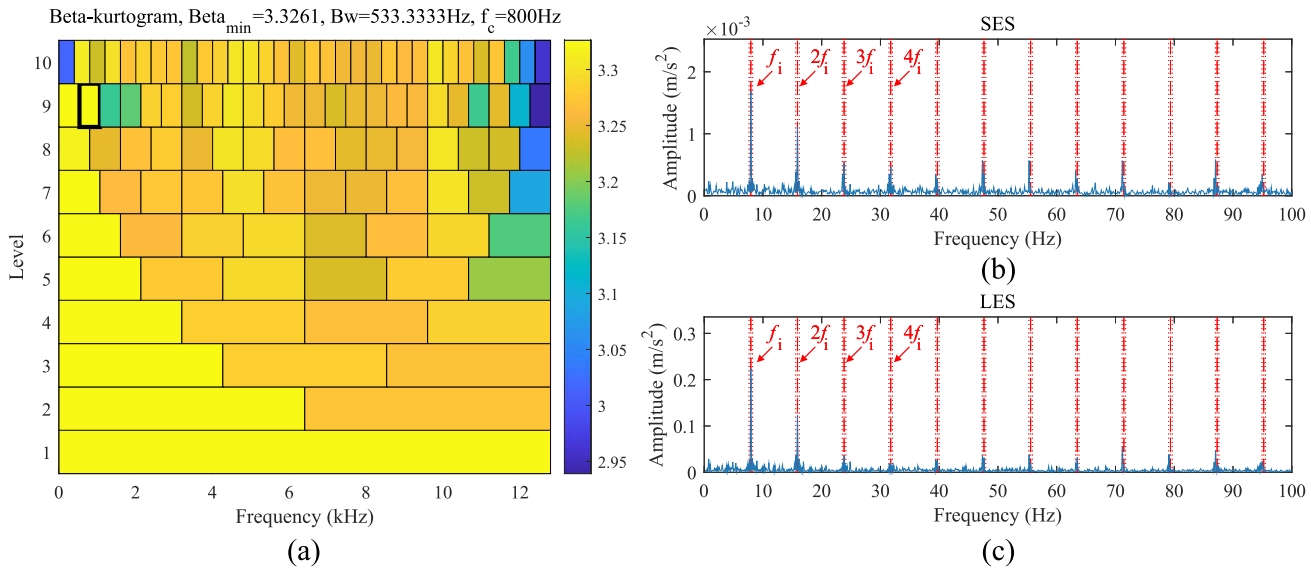

Fig. 12 Signal after post-interference suppression and amplitude limitation: **a** Demodulation band determination via beta-Kurtogram, **b** Squared envelope spectrum, **c** Envelope spectrum in logarithmic scale

the proposed method in monitoring signal state transitions. This is of particular significance in bearing diagnostics scenarios where external noise poses substantial challenges. The successful identification of these characteristic frequencies indicates that the proposed method can effectively extract relevant information from complex signals, thereby enhancing the accuracy and reliability of bearing fault diagnosis in noisy environments.

Unlike deep learning models, the proposed MLFTPR-PM framework ensures complete mathematical transparency through its physically interpretable signal processing stages—from wavelet decomposition to Markov state modeling and weighted periodic thresholding. This interpretability is particularly vital for safety-critical railway bearing diagnostics, where fault root cause analysis is equally important as detection. While deep learning requires substantial training data, our method provides a mathematically rigorous, data-efficient alternative that offers direct insights into system dynamics.

The MLFTPR-PM framework, while involving multiple processing stages, demonstrates manageable computational demand. In the present case study, processing a 20-second

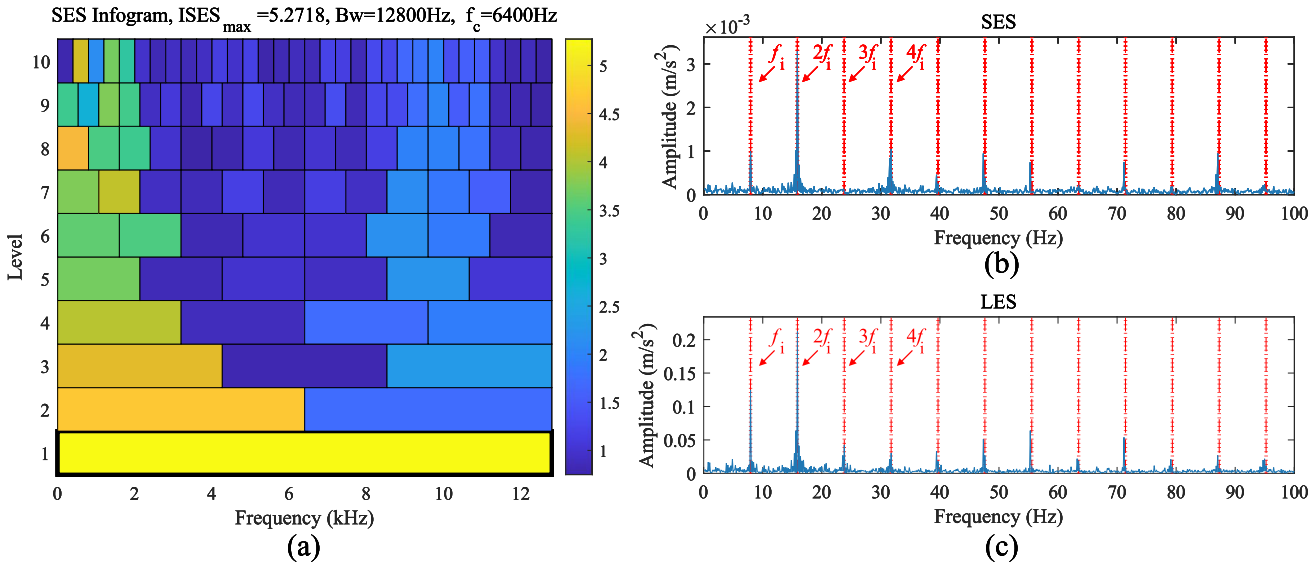

Fig. 13 Signal after post-interference suppression and amplitude limitation: **a** Demodulation band determination via Infogram, **b** Squared envelope spectrum, **c** Envelope spectrum in logarithmic scale

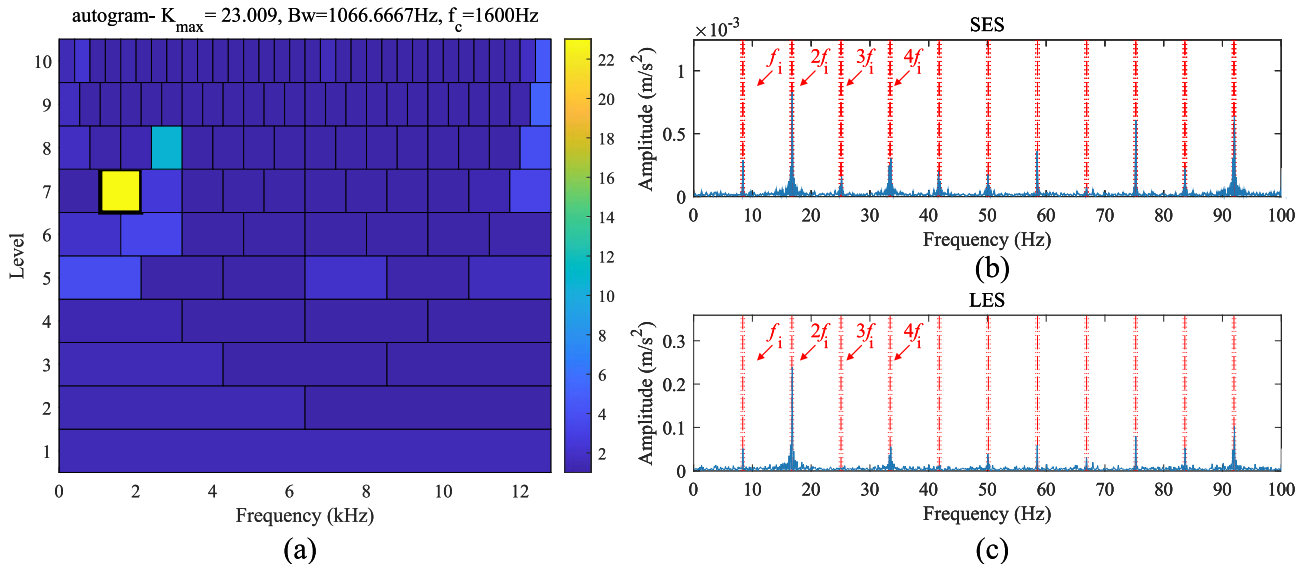

Fig. 14 Signal after post-interference suppression and amplitude limitation: **a** Demodulation band determination via Autogram, **b** Squared envelope spectrum, **c** Envelope spectrum in logarithmic scale

vibration signal sampled at 10,000 Hz required approximately 3.8 s on a standard desktop computer (Intel i7-13700k, 32 GB RAM), with the wavelet decomposition and Markov transition modeling constituting the primary computational load. The algorithm's complexity scales linearly with the signal length, and we anticipate that with code optimization and dedicated hardware, it could achieve near-real-time performance for continuous monitoring in industrial settings, thus affirming its practical applicability.

4.2 Case study II

4.2.1 Test rig setup and data acquisition

The vibration dataset, meticulously collected using a specialized test rig as vividly illustrated in Fig. 15, played a crucial role in validating the effectiveness of the proposed methodology. This test rig was designed with great precision to simulate real world operating conditions as closely as possible. It consists of several key components, including a three phase induction motor, which serves as the prime mover, supplying the necessary rotational energy. A torque meter

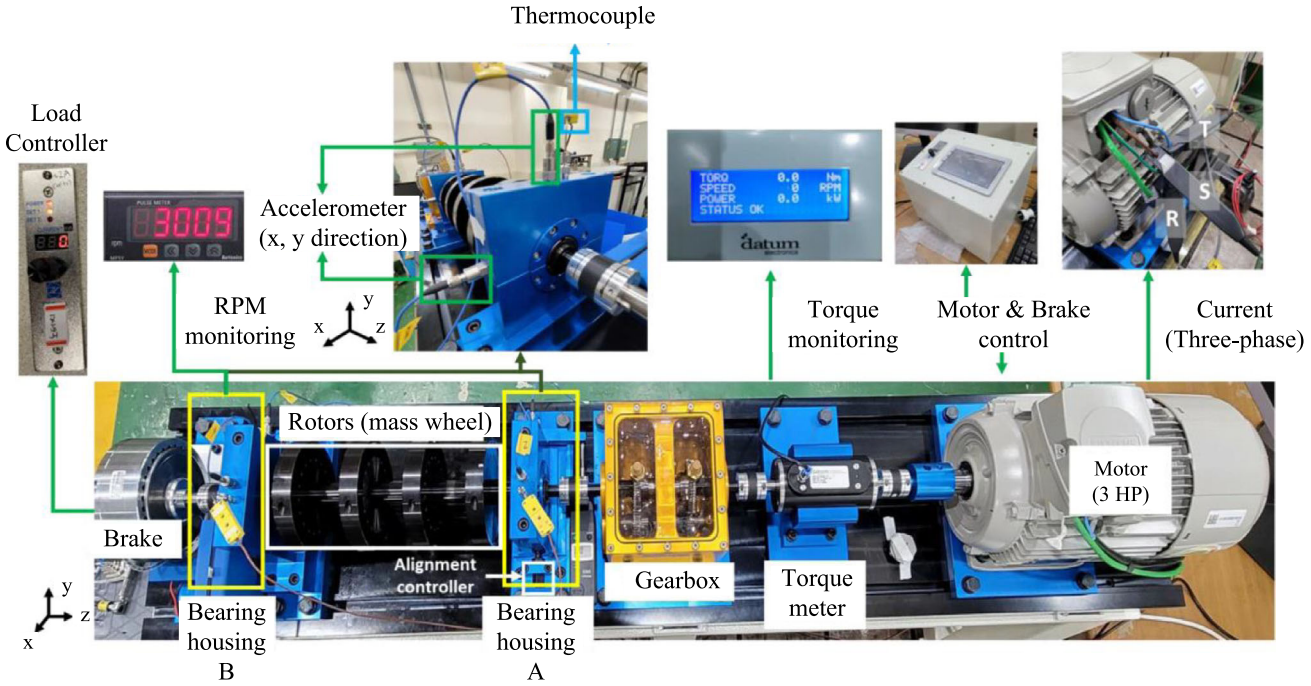

Fig. 15 Experimental testing setup for case study II

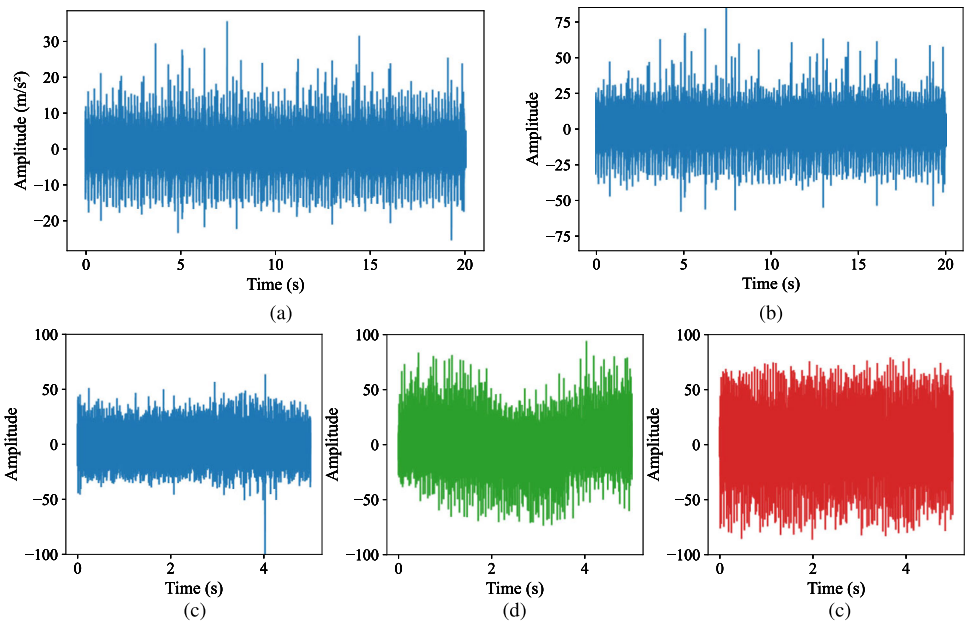

Fig. 16 **a** Raw signal, **b** Level 1 approximation coefficient, **c** Detail coefficient (level 1), **d** Detail coefficient (level 2), and **e** Detail coefficient (level 3) in DWT

is integrated into the setup to accurately measure the torque transmitted through the system. The gearbox, a vital part of the rig, is responsible for transmitting and modulating the rotational speed and torque. It experiences complex mechanical stresses and vibrations during operation, making it a prime source of diagnostic information. Bearing housings A and B house the bearings, providing support and reducing friction for the rotating components. Rotors are integral to the system, contributing to its rotational dynamics. A hysteresis brake is employed to apply variable loads, allowing for the simulation of different operating scenarios. For the experiment, a standardized NSK 6205 DDU bearing was systematically selected and utilized. This bearing has well defined geometric and mechanical characteristics. The bearing incorporates a ball diameter (d) of 7.90 mm, a pitch diameter (D) measuring 38.5 mm, and a contact angle (θ) set at 0 degrees, along with nine (N) balls, all of which determine its unique kinematic and load-carrying properties. These geometric parameters

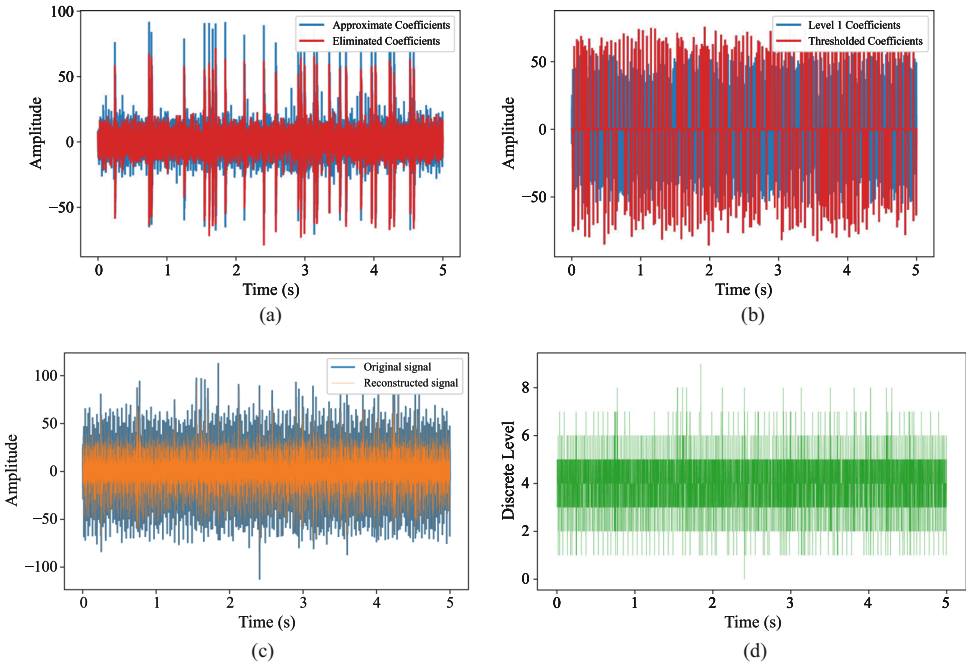

Fig. 17 **a** Low-pass filtered approximation, **b** Thresholded detail coefficients, **c** Equidistant signal discretization, **d** Raw and reconstructed Signals

not only affect the bearing's performance under normal conditions but also influence the vibration patterns generated during fault occurrences.Based on these bearing parameters and the test rig's operational characteristics, specific frequencies emerge during the experiment. The shaft frequency (f_r) registers at 50.17 Hz, serving as a fundamental frequency that reflects the shaft's rotational speed. The fundamental train frequency (FTF) is 19.94 Hz, associated with the overall mechanical system's cyclic behavior. The ball pass frequency for the inner race (BPFI) reaches 272.07 Hz, while the ball pass frequency for the outer race (BPFO) is 179.43 Hz—both critical for detecting inner and outer race faults, respectively. When faults develop in the bearing's inner or outer race, these frequencies exhibit distinct changes in the vibration signal. Additionally, the ball spin frequency (BSF) is 234.19 Hz, linked to the balls' rotation within the bearing and providing valuable insights into the bearing's health. Vibration data are acquired at a relatively high sampling rate of 25600 Hz. This high sampling rate is essential for accurately capturing the complex vibration signals generated by the test rig. A higher sampling rate allows for a more detailed representation of the signal in the time domain, enabling the detection of subtle changes and transient events. It also ensures that all the relevant frequency components within the vibration signal are properly sampled, preventing aliasing and providing a more accurate spectrum analysis. This high quality vibration dataset, with its rich frequency content and high resolution sampling, provides an excellent basis for evaluating the performance of the proposed methodology in accurately diagnosing bearing and gearbox faults.

4.2.2 Experimental validation and comparative analysis

In Case Study 4.2, the collected vibration signals were analyzed using Discrete Wavelet Transform (DWT) for preprocessing decomposition. As shown in Fig. 16, the level 1 approximation coefficients (Fig. 16(b)) effectively capture the low-frequency trends of the raw signal (Fig. 16(a)), while the detail coefficients across levels 1–3 (Fig. 16(c)–(e)) highlight transient features and localized fluctuations critical for fault-related information.

High-frequency components from each decomposition level were further processed via low-pass filtering and thresholding (Fig. 17(a)–(b)), reducing noise and preserving essential signal characteristics. The discretized signal (Fig. 17(c)) and reconstructed output (Fig. 17(d)) enhance the discernibility of anomalous transitions, enabling more accurate detection of signal abnormalities.

A comparative evaluation with conventional methods—STE, STK, and STZCR—illustrates the superior performance of the proposed MLFTPR-PM approach (Fig. 18). While STE (Fig. 18(a)) shows limited sensitivity to minor interferences, STZCR (Fig. 18(b)) is prone to misjudgment under non-stationary noise, and STK (Fig. 18(c)) is susceptible to distortion from non-Gaussian noise. In contrast, MLFTPR-PM (Fig. 18(d)) accurately identifies all transient noise disturbances and maintains robustness against signal anomalies by leveraging Markovian modeling and frequency transition analysis.

Fig. 20 presents dual heatmaps characterizing Markov signal transitions. The frequency heatmap (Fig. 20(a)) reveals persistent state patterns along the diagonal, while off-

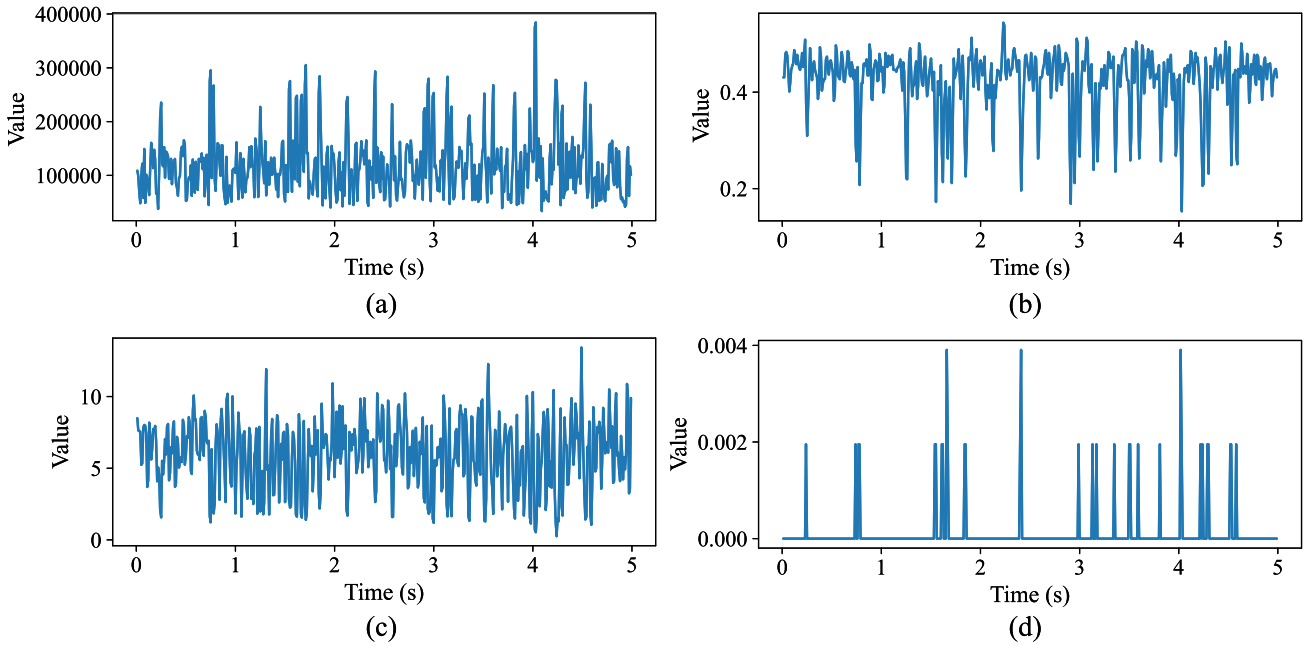

Fig. 18 **a** STE, **b** STZCR, **c** STK, and **d** MLFTPR-PM

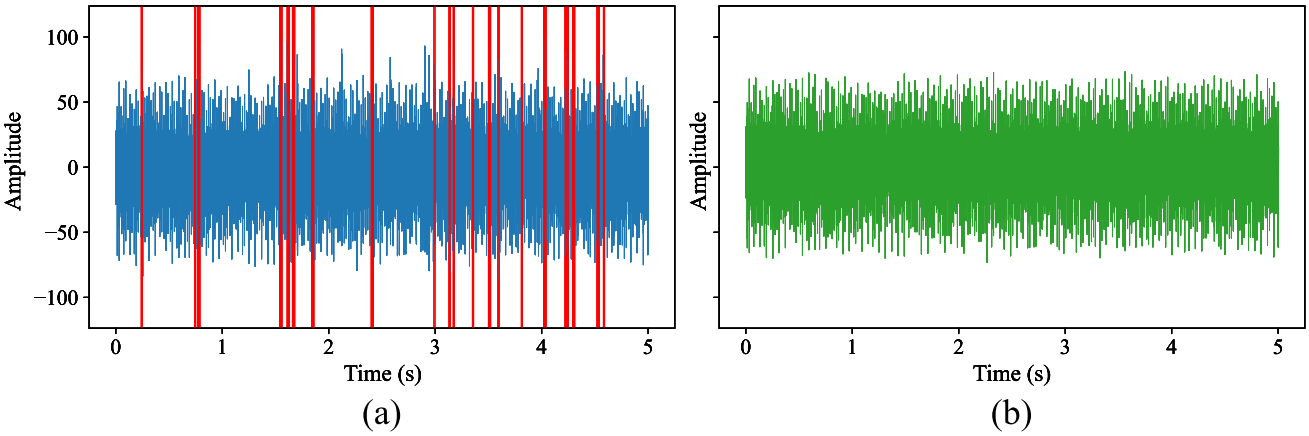

Fig. 19 **a** Signals with interference, **b** Vibration signal with interference suppression

diagonal transitions indicate dynamic signal behavior. Rare anomalies are marked by white-bordered dark zones, with border thickness proportional to transition rarity. The normalized transition probability matrix (Fig. 20(b)) enhances analytical sensitivity by suppressing high-frequency transitions and emphasizing low-frequency patterns. This refined visualization enables detection of subtle transition features not apparent in the original matrix. Integration with the reconstructed signal from Fig. 17(d) allows identification of potential anomaly points. Subsequent application of Eq. 25 enables precise anomaly localization, demonstrating the method's capability for comprehensive Markov signal analysis in complex diagnostic scenarios.

The proposed MLFTPR-PM metric demonstrates effective identification of external transient noise irregularities

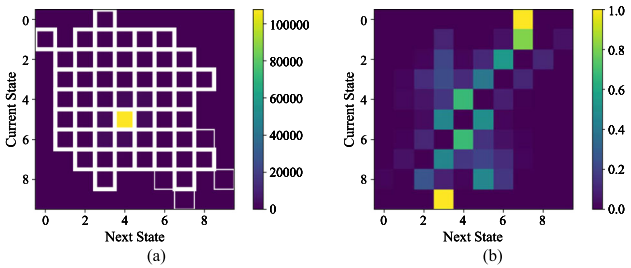

Fig. 20 **a** Markov signal frequencies heat-map, **b** Scaled Markov signal probability heat-map

while maintaining strong interference robustness. As shown in Fig. 19, the comparison between the interfered signal (a) and processed result (b) clearly illustrates the method's

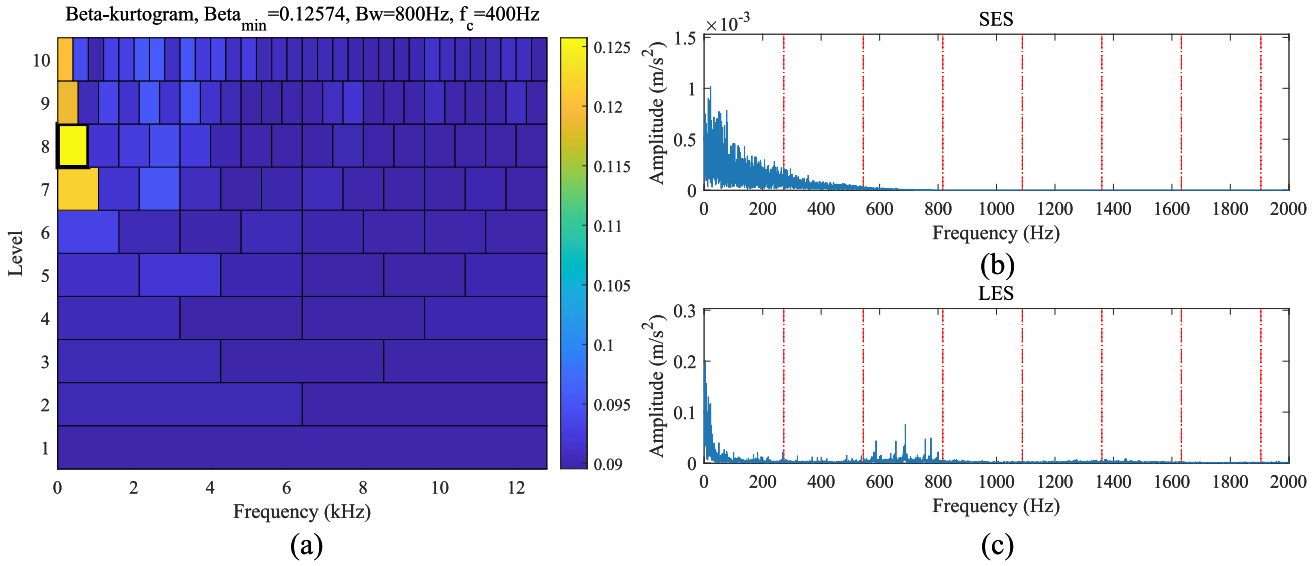

Fig. 21 Raw signal affected by external transient noise interference: (**a**) Demodulation band determination via beta-Kurtogram, (**b**) Squared envelope spectrum, (**c**) Envelope spectrum in logarithmic scale

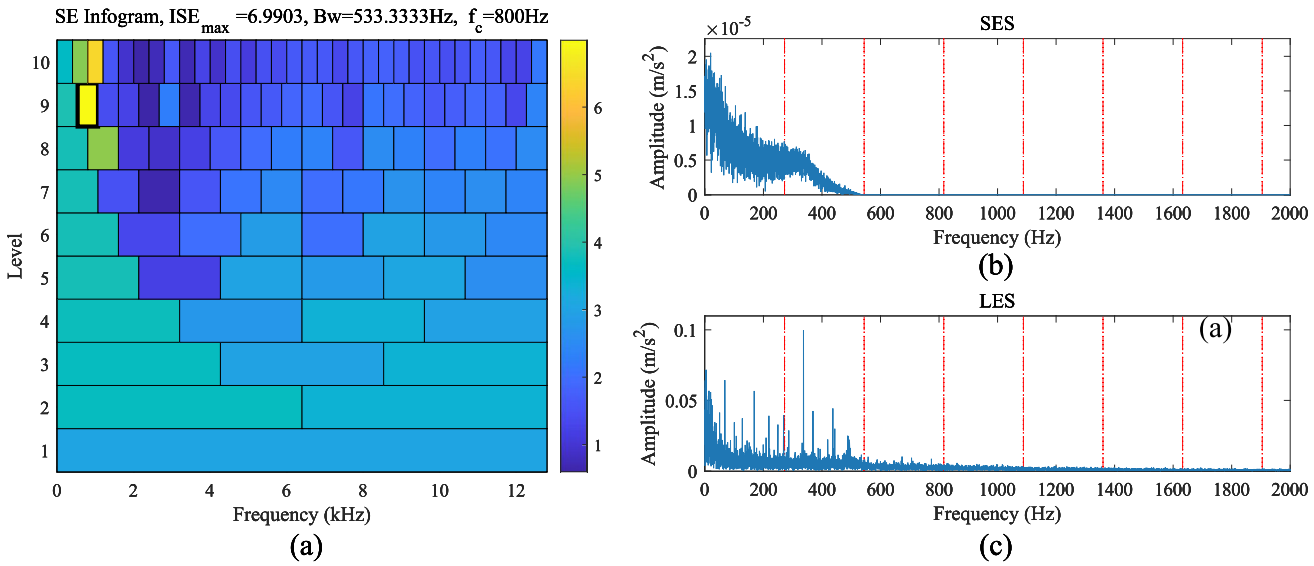

Fig. 22 Raw signal affected by external transient noise interference: (**a**) Demodulation band determination via Infogram, (**b**) Squared envelope spectrum, (**c**) Envelope spectrum in logarithmic scale

capability in suppressing interference while preserving key signal features. Through analysis of transition matrix states and discretized signals, the framework enables estimation of pre-anomaly moments and establishes thresholds for distinguishing normal and abnormal behaviors in low-probability transitions.

In comparative analysis with Kurtogram and Infogram benchmarks applied to raw bearing vibration signals, the methodology demonstrates superior performance in demodulation band selection and envelope analysis following interference suppression and amplitude limitation post-processing.

Fig. 21(a), 22(a), and 23(a) present demodulation band selection results for the original vibration signal, with corresponding SES and LES analyses shown in subsequent subfigures. The conventional methods yield divergent band selections: Kurtogram [400Hz, 800Hz], Infogram [800Hz, 533.3333Hz], and Autogram [266.6667Hz, 533.3333Hz]. Notably, all fail to identify the characteristic frequency f_i = 272.07Hz in their envelope spectra, revealing inherent limitations in traditional approaches for this application scenario.

Following interference suppression processing, the proposed method demonstrates significantly improved demodulation performance (Fig. 24(a), 25(a), 26(a)). The optimized

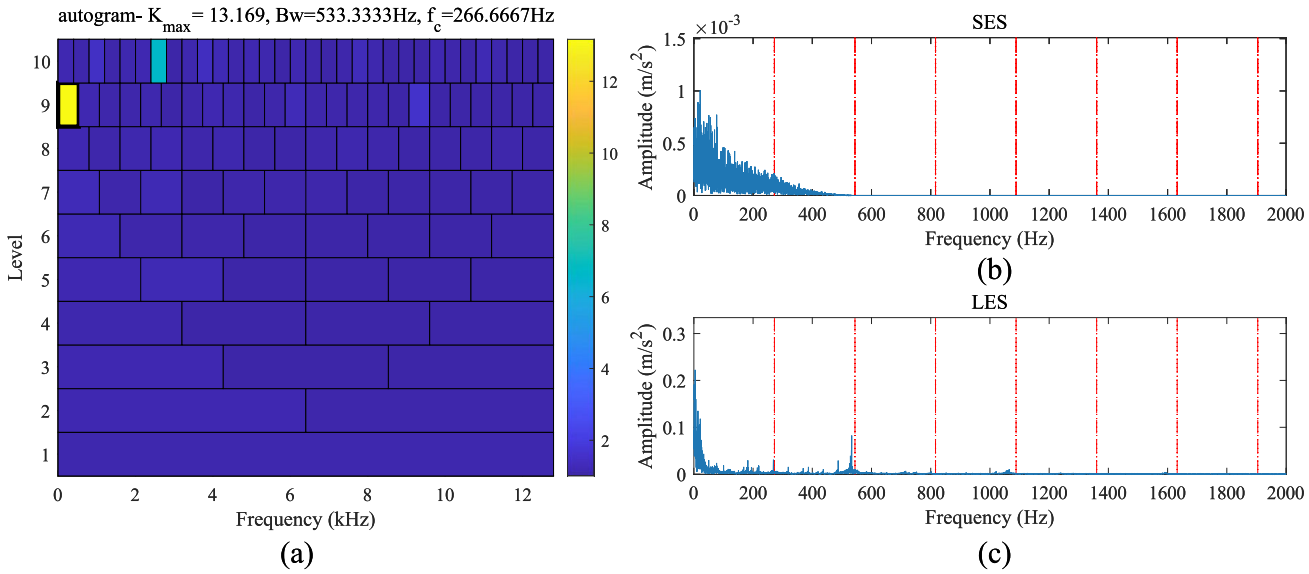

Fig. 23 Raw signal affected by external transient noise interference: (**a**) Demodulation band determination via Autogram, (**b**) Squared envelope spectrum, (**c**) Envelope spectrum in logarithmic scale

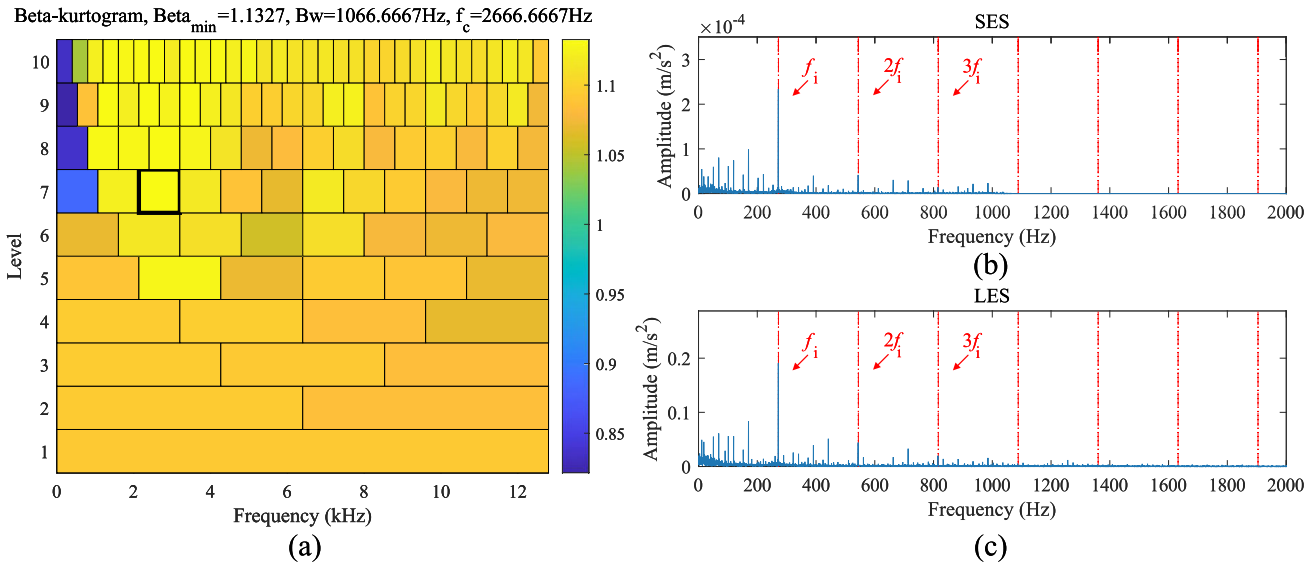

Fig. 24 Signal after post-interference suppression and amplitude limitation: (**a**) Demodulation band determination via beta-Kurtogram, (**b**) Squared envelope spectrum, (**c**) Envelope spectrum in logarithmic scale

band parameters [2666.6667Hz, 1066.6667Hz], [2400Hz, 1600Hz], and [3200Hz, 6400Hz] respectively enable clear identification of characteristic frequencies f_i, $2f_i$, and $3f_i$ in both SES and LES analyses (subfigures b-c). This successful extraction of fault features under noisy conditions validates the method's enhanced capability for reliable bearing diagnosis.

Case Study II demonstrates the method's adaptability to different bearing configurations and operational conditions. The successful identification of characteristic frequencies in the NSK 6205 bearing, which exhibits significantly higher fault frequencies (BPFI = 272.07 Hz) compared to the CRH380B bearing in Case Study I (BPFI = 8.36 Hz), validates the framework's robustness across diverse diagnostic scenarios. This extension to standardized test conditions complements the real-world validation in Case Study I, collectively establishing the method's general applicability.

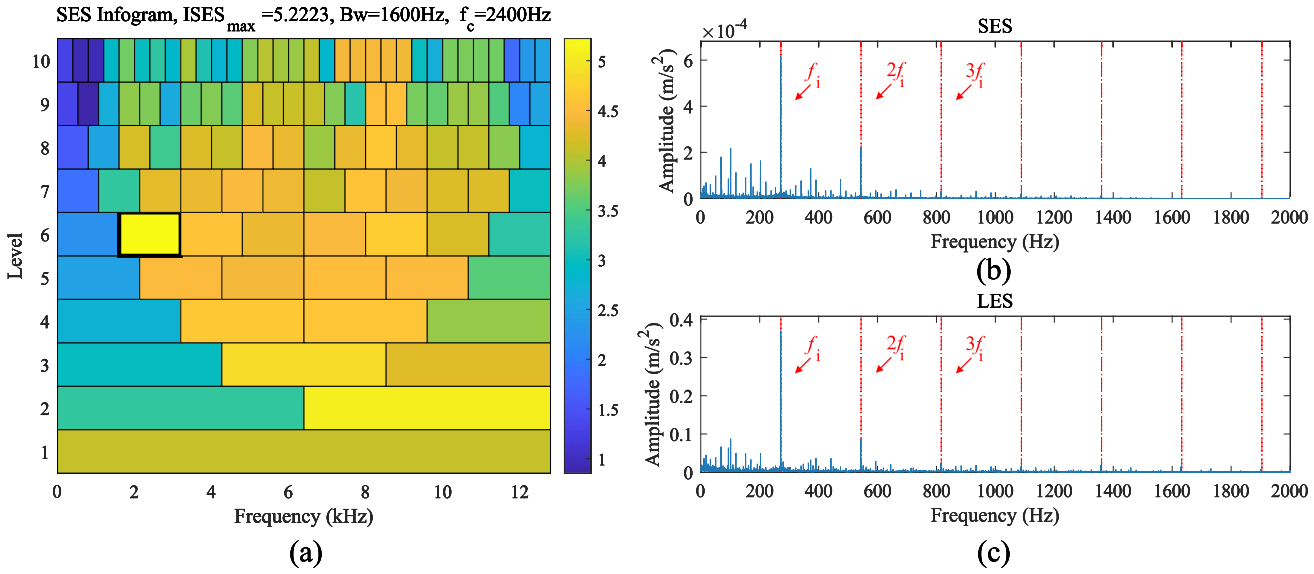

Fig. 25 Signal after post-interference suppression and amplitude limitation: (**a**) Demodulation band determination via Infogram, (**b**) Squared envelope spectrum, (**c**) Envelope spectrum in logarithmic scale

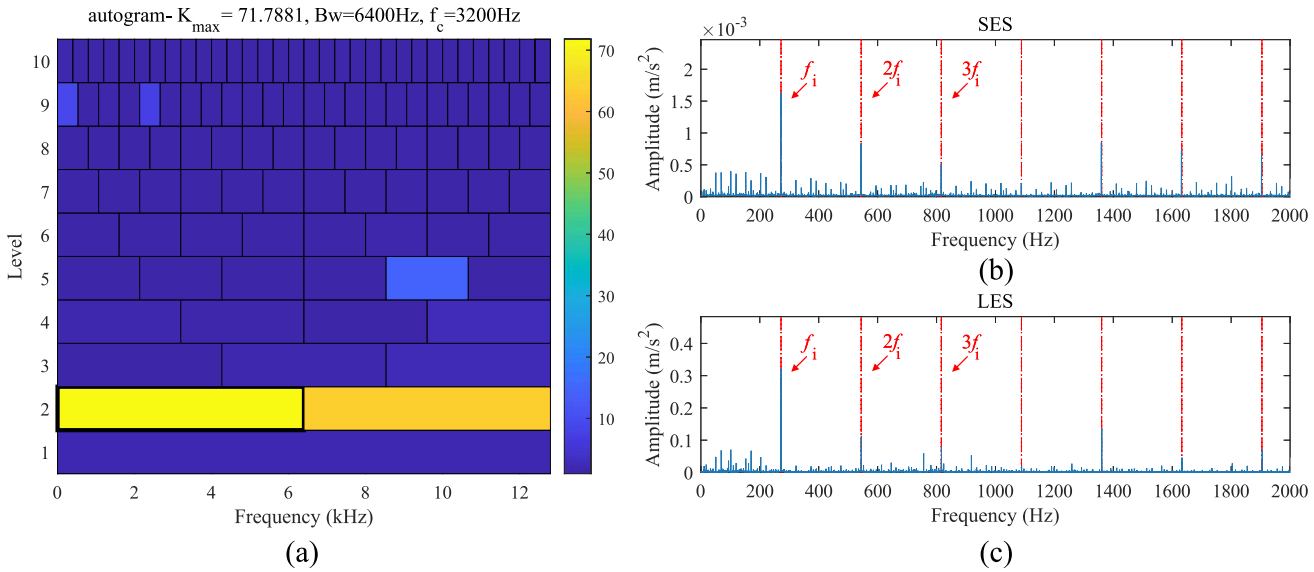

Fig. 26 Signal after post-interference suppression and amplitude limitation: (**a**) Demodulation band determination via Autogram, (**b**) Squared envelope spectrum, (**c**) Envelope spectrum in logarithmic scale

5 Conclusion

This study presents a Markovian spectral transition framework that integrates multi-resolution wavelets and amplitude-adaptive interference suppression to diagnose bogie axle bearing faults under non-stationary, noise-rich conditions. For operators, deployment is straightforward: use existing axlebox vibration and speed signals, compute sliding-window wavelet features, map them to Markov states with dynamic thresholds, and derive a health index that feeds Train Control and Monitoring System (TCMS)/wayside dashboards and Computerized Maintenance Management System (CMMS) for alerts and work orders—either onboard at the edge or wayside in batch. The approach improves robustness to transient, multivariate pulse-like noise and reduces false alarms while remaining compute-efficient and configurable, with interpretable state transitions that support traceable maintenance decisions. Limitations include dependence on sensor placement and minimal context signals, parameter sensitivity, and residual susceptibility to rare extreme impacts; future work will pursue fleet-scale valida-

tion, online/continual adaptation, multi-sensor fusion, and embedded real-time optimization.

Author Contributions Peng Chen: Methodology, Software, Validation, Investigation, Resources, Writing - Original Draft, Writing -Rewiew & Editing, Supervision, Project Administration, Funding Acquistition Junxiao Ma and Jia Tao: Conceptualization, Methodology, Software, Validation, Formal analysis, Investigation, Resources, Data Curation, Writing -Rewiew & Editing, Visualization Ge Xin, and Change He: Conceptualization, Methodology, Software, Validation, Formal analysis, Investigation, Resources, Writing -Rewiew & Editing

Funding This research was supported by the National Natural Science Foundation of China (Grants 52105111, 52375078, U23B20104, 52305085), the Guangdong Basic and Applied Basic Research Foundation (Grant 2025A1515012256), the Shantou University (STU) Scientific Research Initiation Grant (NTF21029), and the Industry-Academia Cooperation Project from the Guangdong Institute of Special Equipment Inspection and Research Shunde Branch (XTJ-KY01-202503-030).

Data Availability Data will be made available on request.

Declarations

Conflict of interest The authors declare that they have no known competing financial interests or personal relationship that could have appeared to influence the work reported in this paper.

References

1. Chen, P., Zhang, R., Fan, S., Guo, J., Yang, X.: Step-wise contrastive representation learning for diagnosing unknown defective categories in planetary gearboxes. Knowl.-Based Syst. **309**, 112863 (2024)
2. Cheng, Y., et al.: An improved envelope spectrum via candidate fault frequency optimization-gram for bearing fault diagnosis. J. Sound Vib. **523**, 116746 (2022)
3. Chen, P., Wu, Y., Xu, C., Jin, Y., Zhou, C.: Markov modeling of signal condition transitions for bearing diagnostics under external interference conditions. IEEE Transactions on Instrumentation and Measurement **73**, 1–8 (2024)
4. Chen, P., et al.: Adaptive signal regime for identifying transient shifts: A novel approach toward fault diagnosis in wind turbine systems. Ocean Eng. **325**, 120798 (2025)
5. Luo, M., Guo, Y., Andre, H., Wu, X., Na, J.: Dynamic modeling and quantitative diagnosis for dual-impulse behavior of rolling element bearing with a spall on inner race. Mech. Syst. Signal Process. **158**, 107711 (2021)
6. He, C., et al.: An improved lightweight residual network model deployed on the edge device for the unsupervised cross-domain fault diagnosis. Expert Syst. Appl. **296**, 129106 (2026)
7. Chen, P. et al. Progressive contrastive representation learning for defect diagnosis in aluminum disk substrates with a bio-inspired vision sensor. Expert Systems with Applications 128305 (2025)
8. Chen, P., et al.: A threshold self-setting condition monitoring scheme for wind turbine generator bearings based on deep convolutional generative adversarial networks. Measurement **167**, 108234 (2021)
9. Xu, C., Chen, P., Gao, J., Jin, Y., Rao, M.: Semi-supervised transfer learning preserving spatial homogeneity for gearbox diagnostics in extraneous transient noise. Nondestructive Testing and Evaluation 1–29 (2025)
10. Wang, Y. et al. Multi-channel fusion scale transformed signals with magnetic leakage for damage detection in steel wire ropes. Nondestructive Testing and Evaluation 1–26 (2025)
11. Ma, J. et al. Markov latent frequency transition analysis for robust bearing diagnosis in transient noise scenarios, 1–8 (IEEE, 2024)
12. Peng, D., et al.: Physics-driven cross domain digital twin framework for bearing fault diagnosis in non-stationary conditions. Mech. Syst. Signal Process. **228**, 112266 (2025)
13. Chen, P. et al. Interference suppression of nonstationary signals for bearing diagnosis under transient noise measurements. IEEE Transactions on Reliability 1–15 (2025)
14. Wu, J., et al.: Semi-supervised fault diagnosis of wheelset bearings in high-speed trains using autocorrelation and improved flow gaussian mixture model. Eng. Appl. Artif. Intell. **132**, 107861 (2024)
15. Chen, P. et al. Physics-aware digital twin and few-shot learning for self-supervised gearbox fault diagnosis. Measurement Science and Technology **36** (2025)
16. Chen, P. et al. Scale-aware domain adaptation for surface defects detection on machine tool components in contaminant measurements. IEEE Transactions on Instrumentation and Measurement 1– 9 (2025)
17. Chen, P., Ma, Z., Xu, C., Jin, Y., Zhou, C.: Self-supervised transfer learning for remote wear evaluation in machine tool elements with imaging transmission attenuation. IEEE Internet Things J. **11**, 23045–23054 (2024)
18. Chen, P., et al.: Metric-guided graph contrastive learning: An unsupervised approach for few-shot gearbox fault diagnosis. Meas. Sci. Technol. **36**, 076110 (2025)
19. Rezazadeh, N., De Oliveira, M., Lamanna, G., Perfetto, D., De Luca, A.: Wavecoral-dcca: A scalable solution for rotor fault diagnosis across operational variabilities. Electronics **14** (2025)
20. Antoni, J., Randall, R.B.: The spectral kurtosis: application to the vibratory surveillance and diagnostics of rotating machines. Mech. Syst. Signal Process. **20**, 308–331 (2006)
21. Han, D., et al.: Adaptive maximum generalized gaussian cyclostationarity blind deconvolution for the early fault diagnosis of high-speed train bearings under non-gaussian noise. Adv. Eng. Inform. **62**, 102731 (2024)
22. Hou, D., et al.: High-speed train wheel set bearing fault diagnosis and prognostics: evaluation of signal processing methods under multi-source interference. Struct. Health Monit. **22**, 2280–2304 (2023)
23. Wang, C., Qi, H., Hou, D., Han, D., Yang, J.: Ensefgram: An optimal demodulation band selection method for the early fault diagnosis of high-speed train bearings. Mech. Syst. Signal Process. **213**, 111346 (2024)
24. He, C., et al.: Weak fault feature extraction in non-gaussian noise interference based on adaptive recombination empirical wavelet transform incorporated by sparse coding shrinkage. Meas. Sci. Technol. **36**, 036119 (2025)
25. Pancaldi, F., Dibiase, L., Cocconcelli, M.: Impact of noise model on the performance of algorithms for fault diagnosis in rolling bearings. Mech. Syst. Signal Process. **188**, 109975 (2023)
26. Yang, J., Sun, R., Yao, D., Wang, J., Wei, M.: Research on rolling bearing fault diagnosis method based on harmonic noise kurtosis-time characteristic blind deconvolution. IEEE Trans. Instrum. Meas. **73**, 1–15 (2024)
27. Peng, D., Zhu, X., Teng, W., Liu, Y.: Use of generalized gaussian cyclostationarity for blind deconvolution and its application to bearing fault diagnosis under non-gaussian conditions. Mech. Syst. Signal Process. **196**, 110351 (2023)
28. Chen, P., et al.: Adaptive signal regime for identifying transient shifts: A novel approach toward fault diagnosis in wind turbine systems. Ocean Eng. **325**, 120798 (2025)

29. Gabor, M., Zdunek, R., Zimroz, R., Wylomanska, A.: Bearing damage detection with orthogonal and nonnegative low-rank feature extraction. IEEE Trans. Industr. Inf. **20**, 2944–2955 (2024)
30. Schirmer, P. A., Mporas, I.: Energy disaggregation from low sampling frequency measurements using multi-layer zero crossing rate, 3777–3781 (IEEE, 2020)
31. Alimi, S., Awodele, O.: Voice activity detection: Fusion of time and frequency domain features with a svm classifier. Comput. Eng. Intell. Syst **13**, 20–29 (2022)
32. Chen, B., Hu, Y., Wu, L., Li, H.: Partial Discharge Pulse Extraction and Interference Suppression Under Repetitive Pulse Excitation Using Time-Reassigned Multi-Synchrosqueezing Transform. IEEE Transactions on Instrumentation and Measurement 1–9 (2023)
33. Daubechies, I., Sweldens, W.: Factoring wavelet transforms into lifting steps. Wavelets in the Geosciences 131–157 (2005)
34. Daubechies, I.: The wavelet transform, time-frequency localization and signal analysis. IEEE Trans. Inf. Theory **36**, 961–1005 (1990)
35. Antoni, J.: The infogram: Entropic evidence of the signature of repetitive transients. Mech. Syst. Signal Process. **74**, 73–94 (2016)